

DRUM: Diffusion-based runoff model for probabilistic flood forecasting

Zhigang Ou^{*, 1, 2}, Congyi Nai^{*, 2}, Baoxiang Pan^{** , 2}, Ming Pan³, Chaopeng Shen⁴, Peishi Jiang⁵, Xingcai Liu⁶, QiuHong Tang⁶, Wenqing Li⁷, Yi Zheng^{** , 1}

¹ School of Environmental Science and Engineering, Southern University of Science and Technology, Shenzhen, China

² Key Laboratory of Earth System Numerical Modeling and Application, Institute of Atmospheric Physics, Chinese Academy of Science, Beijing, China

³ Scripps Institution of Oceanography, University of California San Diego, La Jolla, CA, USA

⁴ Civil and Environmental Engineering, The Pennsylvania State University, University Park, PA

⁵ Atmospheric, Climate, and Earth Sciences Division, Pacific Northwest National Laboratory, Richland, WA, USA

⁶ Key Laboratory of Water Cycle and Related Land Surface Processes, Institute of Geographic Sciences and Natural Resources Research, Chinese Academy of Sciences, Beijing, China

⁷ State Key Laboratory of Stimulation and Regulation of Water Cycles in River Basins, China Institute of Water Resources and Hydropower Research, Beijing, China

*Equal contribution.

**Corresponding author(s). Email(s): zhengyi@sustech.edu.cn; panbaoxiang@lasg.iap.ac.cn

Abstract

Reliable flood forecasting remains a critical challenge due to persistent underestimation of peak flows and inadequate uncertainty quantification in current approaches. We present DRUM (Diffusion-based Runoff Model), a generative AI solution for probabilistic runoff prediction. DRUM builds up an iterative refinement process that generates ensemble runoff estimates from noise, guided by past meteorological conditions, present meteorological forecasts, and static catchment attributes. This framework allows learning complex hydrological behaviors without imposing explicit distributional assumptions, particularly benefiting extreme event prediction and uncertainty quantification. Using data from 531 representative basins across the contiguous United States, DRUM outperforms state-of-the-art deep learning methods in runoff forecasting regarding both deterministic and probabilistic skills, with particular advantages in extreme flow (1%) predictions. DRUM demonstrates superior flood early warning skill across all magnitudes and lead times (1–7 days), achieving F1 scores near 0.4 for extreme events under perfect forecasts and maintaining robust performance with operational forecasts, especially for longer lead times and high-magnitude floods. When applied to climate projections through the 21st century, DRUM reveals increasing flood vulnerability in 47.8–57.1% of basins across emission scenarios, with particularly elevated risks along the West Coast and Southeast regions. These advances demonstrate significant potential for improving both operational flood forecasting and long-term risk assessment in a changing climate.

1. Introduction

Floods rank among the deadliest natural disasters, claiming 6.8 million lives in the 20th century alone¹. Their devastating impact continues to intensify, with flood-related disasters increasing by 134% since 2000 and causing over 100,000 deaths and USD 651 billion in economic losses². This intensification stems from both increasing flood frequency^{3,4}, and continued urban development in flood-prone areas⁵. While flood forecasting provides critical disaster preparedness capabilities, reliable forecasting remains a fundamental challenge, due to persistent underestimation of peak flows and inadequate uncertainty quantification in current approaches^{6,7,8,9}. These limitations severely impair our ability to issue trustworthy flood warnings, as underestimating extreme events, or issuing over-confident deterministic predictions can mislead decision making and emergency responses. Despite recent advances in flood forecasting driven by observational, modeling, and computational progresses^{10,11,12,13}, the critical challenges of peak flow underestimation and uncertainty quantification persist, calling for urgent attention to enable more reliable flood forecasting.

Deep Learning (DL) has revolutionized rainfall-runoff modeling by leveraging extensive historical data^{14,15,16,17,18,19}, with Long Short-Term Memory (LSTM) networks achieving unprecedented predictive accuracy. Meanwhile, uncertainty quantification in hydrological modeling has not considerably benefited from big data, and still largely relies on traditional approaches — including parameterized probability distribution fitting methods²⁰, Monte Carlo sampling techniques^{21,22}, and approximate Bayesian computation^{23,24}. These approaches are often limited by restrictive assumptions in characterizing process stochasticity, whether through rigid distributional assumptions, sampling convergence limitations, or likelihood-free approximations. While deterministic DL models show promise in prediction, they inherit these limitations in uncertainty quantification. Recent advances in probabilistic DL offer a paradigm shift by directly parameterizing runoff probability distributions²⁵, enabling end-to-end learning of process uncertainties.

Here, we push the boundaries of flood forecasting accuracy and uncertainty quantification by leveraging probabilistic diffusion model^{26,27}, a cutting-edge technique in generative AI. We develop the diffusion-based runoff model (DRUM) for probabilistic runoff prediction, given conditioning information from meteorological forcings and static catchment features. During training, DRUM defines a stochastic process that progressively erases high-frequency information in runoff sequences²⁸. We then train a hierarchy of deep neural networks to sequentially reconstruct low-to-high frequency signals, starting from random noise, ending with probabilistic runoff estimate. This framework offers two key advantages. First, it decomposes the challenging task of probabilistic runoff prediction into manageable sub-tasks, where each neural net specializes in pattern recovery at a specific temporal scale. Second, it maintains strict physical consistency by enforcing meteorological and catchment constraints across all scales of prediction. Through this combination of multi-scale learning and physical constraint enforcement, DRUM can potentially capture the full spectrum of possible runoff scenarios. This makes the model

particularly adept at predicting extreme events and complex hydrological responses without requiring explicit assumptions about probability distributions.

We evaluate DRUM against state-of-the-art benchmarks, including a deterministic LSTM (LSTM-d)¹⁵ and a probabilistic LSTM (LSTM-p)¹⁰ across the contiguous United States (CONUS) using the Catchment Attributes and MEteorology for Large-sample Studies (CAMELS)^{29,30}. DRUM demonstrates superior nowcasting (0-day lead time) performance compared to these benchmarks, particularly in capturing high flows and extreme events, while providing well-calibrated uncertainty estimates. In operational forecasting settings (1–7-day lead times), DRUM consistently outperforms LSTM-based models across flood magnitudes under both perfect weather forecasts and the European Centre for Medium-Range Weather Forecasts Integrated Forecasting System (ECMWF-IFS) reforecasts. Furthermore, our analysis of future climate scenarios using NASA Earth Exchange Global Daily Downscaled Projections (NEX-GDDP-CMIP6)³¹ reveals that higher emission pathways lead to increased flood risks, with particularly pronounced impacts in vulnerable regions such as the West Coast and Southeast regions.

2. Forecast skill in extreme runoff events

Diffusion models have recently achieved significant success in fields such as computer vision and natural language processing^{32,33}, largely due to their ability to progressively denoise random signals into structured data through a theoretically-grounded probabilistic framework, enabling the generation of high-quality outputs. Our approach, DRUM, a conditional diffusion model for probabilistic runoff forecasting (Methods), outperforms state-of-the-art LSTM-based benchmarks in extreme runoff nowcasting (Fig. 1), as measured by the Continuous Ranked Probability Score (CRPS; see Methods) for the top 1% of flows. After training and testing on the CAMELS dataset, DRUM demonstrates superior probabilistic skill under high-flow conditions, surpassing LSTM-p in 72.3% of the 531 studied basins (Fig. 1a) and LSTM-d in 76.3% (Supplementary Fig. S1), as reflected by its lower CRPS values. All comparisons show statistical significance (paired Wilcoxon tests, $p < 0.01$). In terms of deterministic skills, the ensemble mean prediction (50 members) of DRUM achieves higher performance with median Kling–Gupta efficiency (KGE) improving from 0.779 (LSTM-d) to 0.822 and median Nash–Sutcliffe efficiency (NSE) from 0.770 (LSTM-p) to 0.788 across basins (Table 1), where LSTM-d shows stronger KGE while LSTM-p exhibits better NSE among baselines.

In addition, DRUM achieves a near-symmetrical error distribution in the bias of flow duration curve high-segment volume (FHV) for the top 1% of flows (49.0% of basins positive, 51.0% negative), whereas LSTM-p and LSTM-d exhibit negative skewness (Fig. 1b), reflecting their tendency to underestimate extreme flows. DRUM's superior performance is particularly evident in eight extreme flood events that exceeded all training data magnitudes (Figs. 1c-j). The model's ensemble mean predictions closely align with observed peak flows, with the 95% prediction intervals (PIs) effectively encompassing the observed flow trajectories. In contrast, both LSTM models severely underestimate flow peaks, and LSTM-p generates overly wide 95% PIs that compromise the practical utility of its probabilistic forecasts.

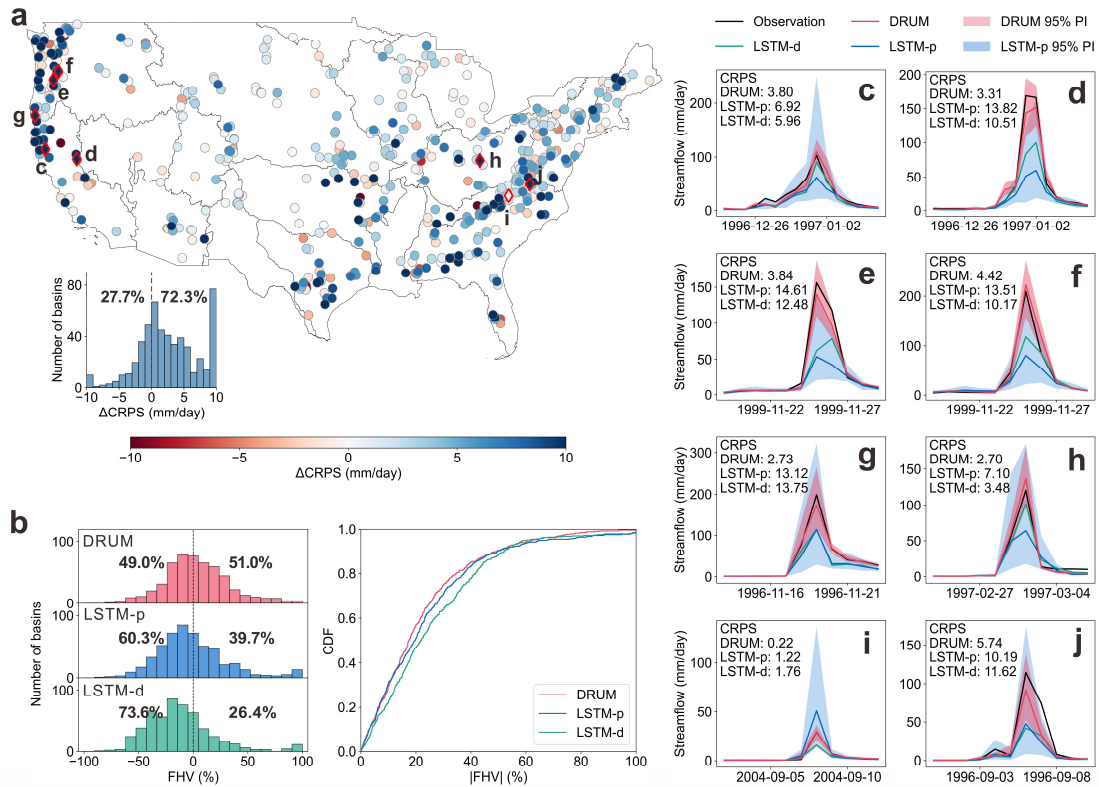


Fig. 1. Enhanced model performance for extreme runoff forecasting across 531 representative basins in the conterminous United States (CONUS). **a**, Comparing Continuous Ranked Probability Score (CRPS) between DRUM and LSTM-p for the top 1% of flow events. Positive Δ CRPS (LSTM-p minus DRUM) indicates better performance by DRUM. Inset shows the Δ CRPS distribution truncated to $[-10, 10]$ for visualization clarity. **b**, Distribution of the bias in high-segment volume (FHV) for the top 1% of flows, where positive and negative values indicate over- and underestimation respectively. The cumulative distribution function (CDF) of absolute FHV demonstrates the accuracy across the spectrum, showing consistently lower bias magnitudes for DRUM compared to both LSTM variants. **c-j**, Forecasts of top-ranked flow peaks in locations marked in Fig. 1a. Solid lines represent ensemble means for probabilistic models (DRUM and LSTM-p) and point forecasts for the deterministic model (LSTM-d), with shaded areas showing 95% prediction intervals (PIs) for probabilistic models.

Table 1. Median basin-level performance metrics across models. For probabilistic models (DRUM and LSTM-p), deterministic predictions are computed by averaging 50 samples. Error bounds indicate the 25th and 75th percentiles across basins.

	DRUM	LSTM-p	LSTM-d	Range	Optimal
KGE ^a	0.822 ^{+0.056} _{-0.106}	0.750 ^{+0.092} _{-0.103}	0.779 ^{+0.070} _{-0.129}	$[-\infty, 1]$	1
NSE ^b	0.788 ^{+0.066} _{-0.103}	0.770 ^{+0.060} _{-0.105}	0.768 ^{+0.068} _{-0.100}	$[-\infty, 1]$	1
α -NSE ^c	1.006 ^{+0.090} _{-0.101}	0.906 ^{+0.118} _{-0.131}	0.945 ^{+0.119} _{-0.108}	$[0, \infty]$	1
β -NSE ^d	0.012 ^{+0.042} _{-0.034}	-0.010 ^{+0.043} _{-0.055}	0.005 ^{+0.048} _{-0.050}	$[-\infty, \infty]$	0
MAE ^e	0.360 ^{+0.140} _{-0.110}	0.375 ^{+0.159} _{-0.118}	0.405 ^{+0.158} _{-0.123}	$[0, \infty]$	0
COR ^f	0.904 ^{+0.029} _{-0.038}	0.897 ^{+0.029} _{-0.045}	0.896 ^{+0.031} _{-0.040}	$[-1, 1]$	1
FHV ^g	0.608 ^{+19.782} _{-15.623}	-15.453 ^{+17.010} _{-17.969}	-5.552 ^{+20.128} _{-16.480}	$[-\infty, \infty]$	0
FLV ^h	14.654 ^{+27.553} _{-22.561}	16.713 ^{+32.924} _{-28.582}	16.367 ^{+35.301} _{-58.696}	$[-\infty, \infty]$	0
FMS ⁱ	-1.500 ^{+5.730} _{-5.930}	-1.042 ^{+8.320} _{-7.654}	-9.801 ^{+12.959} _{-14.919}	$[-\infty, \infty]$	0
P-T ^j	0.316 ^{+0.284} _{-0.125}	0.353 ^{+0.314} _{-0.148}	0.357 ^{+0.300} _{-0.135}	$[-\infty, \infty]$	0

^a Kling–Gupta Efficiency. ^b Nash–Sutcliffe Efficiency. ^c Variability term of NSE. ^d Bias term of NSE. ^e Mean Absolute Error. ^f Pearson correlation. ^g Bias of top 1% peak flows. ^h Bias of bottom 30% low flows. ⁱ Bias of middle segment flows. ^j Peak timing lag.

We further investigate the uncertainty estimates of probabilistic forecasting models based on their 95% PIs. DRUM and LSTM-p demonstrate strongly correlated uncertainty estimates (Pearson’s $r > 0.8$ in $\sim 80\%$ of basins), with both models showing consistent positive correlations between uncertainty magnitude and precipitation intensity (Fig. 2a, Supplementary Fig. S2). This alignment under identical hydrological conditions suggests comparable capabilities in capturing process complexity. However, spatial analysis using a scaling factor k ($\text{DRUM} = k \times \text{LSTM-p}$) reveals that DRUM produces more concentrated uncertainty estimates relative to LSTM-p (Fig. 2b). This feature, coupled with DRUM’s superior forecast accuracy, indicates simultaneous achievement of higher prediction skill and more precise uncertainty quantification. The advantages become particularly evident in extreme flood peaks exceeding the training data range (Fig. 2c-j), where DRUM generating sharper probability distributions centered around observed values, while LSTM-p produces notably wider distributions. These findings demonstrate DRUM’s reliable uncertainty estimates across all flow conditions, marking a crucial advancement for operational flood forecasting.

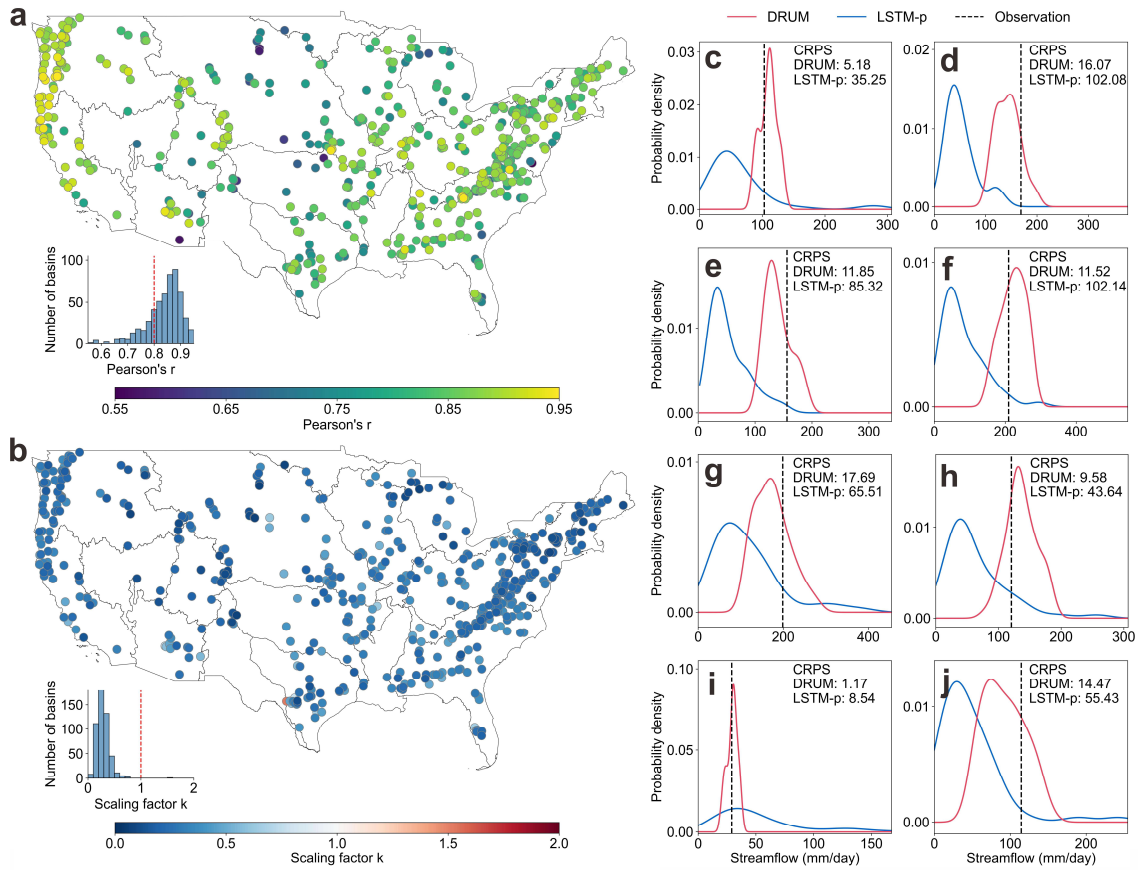


Fig. 2. Probabilistic models for uncertainty quantification in rainfall-runoff prediction. **a**, Spatial distribution of correlation (Pearson's r) between uncertainty estimates from DRUM and LSTM-p. Inset shows distribution of r values, with all basins showing statistical significance ($p < 0.01$, two-tailed Student's t -test). **b**, Spatial distribution of scaling factor (k), where $k < 1$ indicates more concentrated uncertainty estimates from DRUM ($p < 0.01$, two-tailed Student's t -test). **c-j**, Probability distributions of peak discharge forecasts during extreme floods. Basin locations and flood events correspond to Fig. 1a and 1c-j.

3. Operational flood forecasting

Building on DRUM's success in nowcasting, we extend its operational flood forecasting capability using precipitation forecasts from an operational weather forecasting model (ECMWF-IFS). We generate 7-day streamflow predictions with DRUM and LSTM-based models using both perfect forcing (observed precipitation) and ECMWF-IFS forecasts across two representative cases: a 5-year flood (Fig. 3a) and a 50-year flood (Fig. 3b). While all models exhibit similar response patterns to precipitation, DRUM shows superior prediction accuracy across magnitudes (Fig. 3). Under perfect forcing, all models capture the 5-year flood dynamics effectively, while only DRUM accurately reproduces both timing and magnitude of the 50-year flood peak, with LSTM-based models showing significant underestimation. When driven by ECMWF-IFS forecasts, DRUM maintains predictive skill up to 7 days ahead of the 5-year flood peak and provides effective 1-day

warning for the 50-year flood, whereas LSTM-based models are limited to 2-day and near-zero lead times, respectively. Analysis of F1 scores across flood magnitudes and lead times (Fig. 4) demonstrates DRUM’s consistent superiority over LSTM-based models. DRUM outperforms baselines across all return periods and lead times, with performance differences most pronounced for extreme events (e.g., 20- and 50-year return periods). Under perfect precipitation forecasts (Fig. 4a), DRUM sustains F1 scores near 0.4 for these events, while LSTM models rapidly degrade. Even with operational ECMWF-IFS forecasts (Fig. 4b), DRUM maintains significantly higher F1 scores, exhibiting slower performance decline across lead times (1–7 days) compared to the steep losses observed in LSTM models. These results highlight DRUM’s robustness and its capacity to deliver reliable predictions for both extreme floods and operational forecasting scenarios

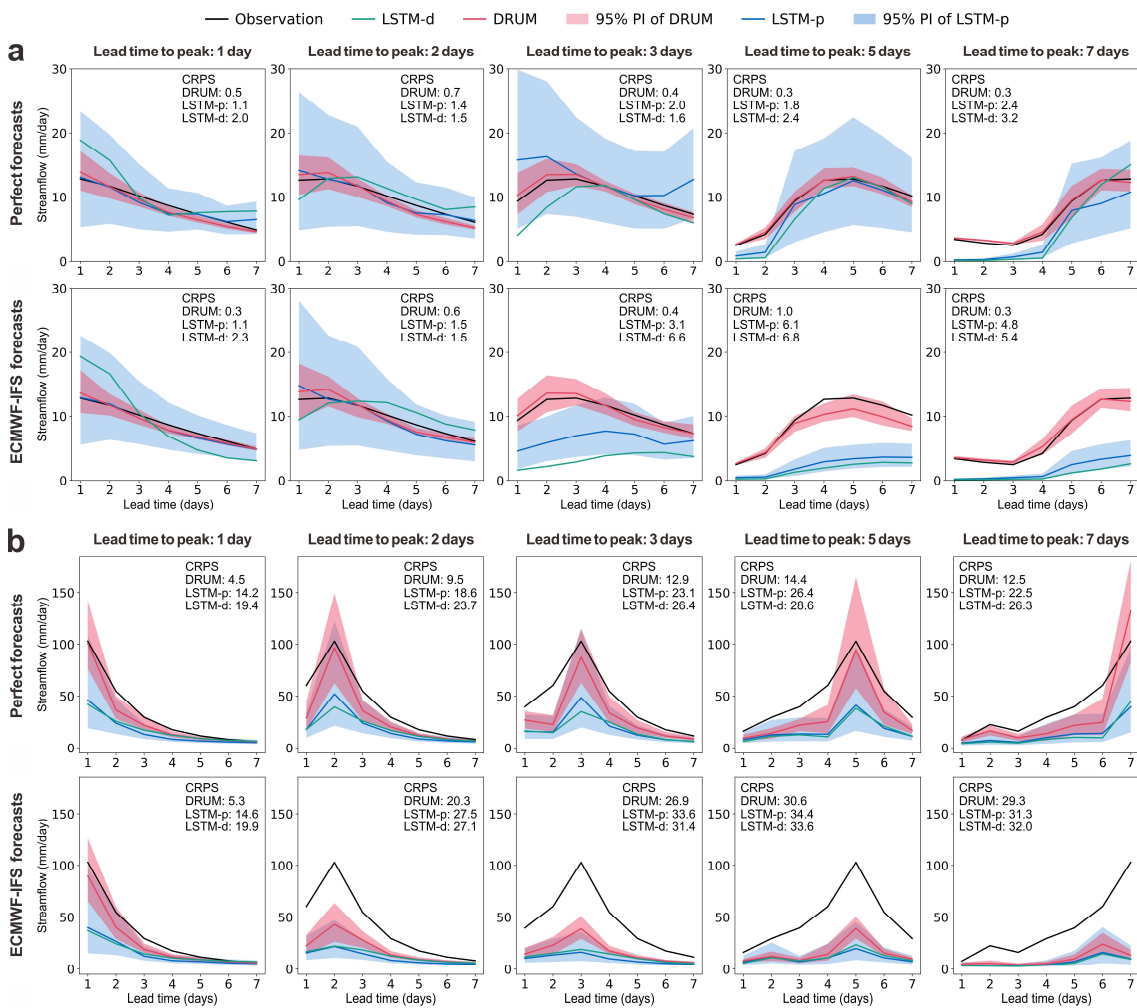


Fig. 3. Case studies of 7-day streamflow forecasts driven by perfect and ECMWF-IFS precipitation forecasts. a,b, Comparison of a 5-year flood (a) and a 50-year flood (b), showing lead times of 1–7 days before the flood peak. For each subplot, the upper and lower panels show forecasts driven by perfect precipitation and ECMWF-IFS forecasts, respectively. Solid lines represent ensemble means (DRUM and LSTM-p) or deterministic forecasts (LSTM-d), with shaded areas showing 95% PIs. CRPS values for the 7-day flood events are shown in the panels.

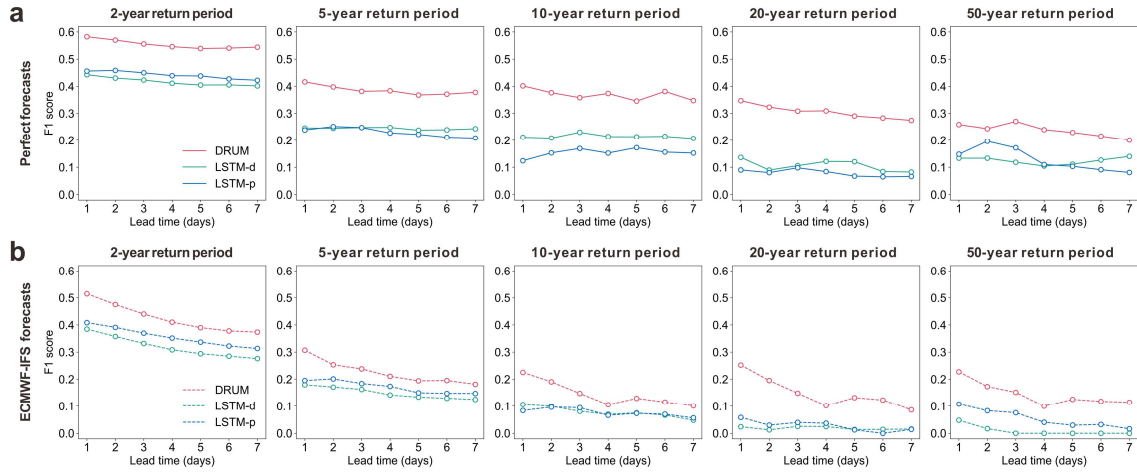


Fig. 4. Flood forecasting performance across different return periods. a,b, F1 score evolution with lead time for floods of varying magnitudes (2- to 50-year return periods), using perfect precipitation (a) and ECMWF-IFS precipitation forecasts (b).

To quantify the impact of precipitation forecast quality on operational flood forecasting, we evaluate flood forecasting skill for return-period-based flood events using precision and recall, then assess early warning capability using mean lead time, which represents the average maximum forecast lead time across all flood events within each basin (Methods). DRUM achieves precision scores of 0.2–0.5 across return periods, decreasing with higher-magnitude events (Fig. 5a). The potential for improvement in precision, measured by the gap between perfect and ECMWF-IFS precipitation forecasts, spans 0.02 to 0.14 at 7-day lead time. For recall scores (Fig. 5b), DRUM sustains values near 0.5 with perfect forecasts but decreases to 0.1–0.3 with ECMWF-IFS forecasts, indicating greater potential for improvement (Δ Recall: 0.26–0.44) primarily due to systematic precipitation underestimation (Supplementary Fig. S3). This recall sensitivity is particularly valuable for operational forecasting, where missed floods pose greater risks than false alarms. Spatially, flood warning capabilities vary markedly across regions. Under perfect forecasts, the West Coast and Southeast regions achieve 5–7-day warning times, while the Midwest regions exhibit shorter lead times (Fig. 5c). The Δ mean lead time distribution (Fig. 5d), computed as the difference between perfect and ECMWF-IFS forecast-driven predictions, identifies regions where improved precipitation forecasts would yield the greatest benefits. Similarly, the West Coast and Southeast regions demonstrate the greatest potential, suggesting that enhanced precipitation forecast accuracy could extend warning times by 3–7 days.

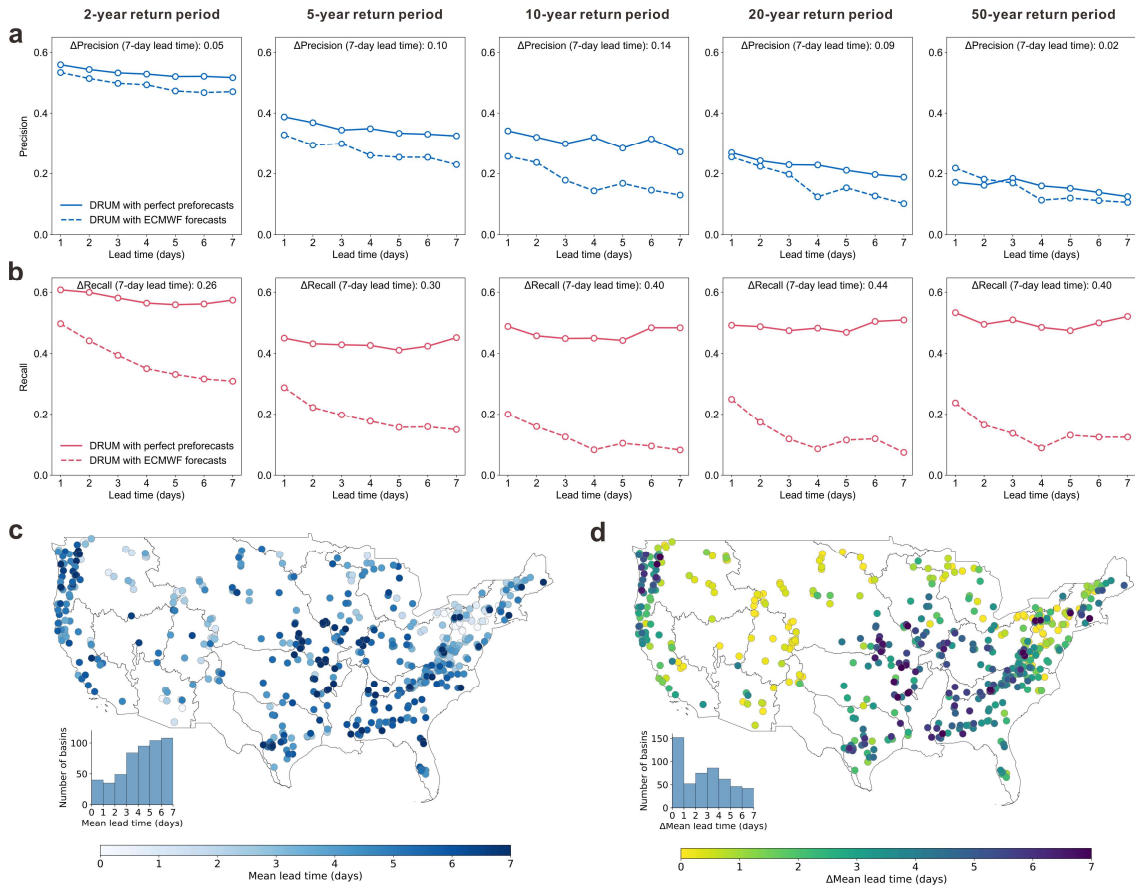


Fig. 5. Impact of precipitation forecast quality on flood forecasting skill and early warning capability. **a,b,** Performance evaluation across flood return periods (2-, 5-, 10-, 20-, and 50-year), showing precision (**a**) and recall (**b**) from 1- to 7-day forecasts. Solid and dashed lines show predictions driven by perfect and ECMWF-IFS precipitation forecasts respectively, with Δ Precision and Δ Recall indicating their differences at 7-day lead time. **c,d,** Spatial distribution of flood early warning capability, showing mean lead time under perfect forecasts (**c**) and potential improvements (**d**). Inset histograms show the distribution of mean lead times.

4. Intensified flood risks under climate change

Understanding future flood risk is crucial for climate adaptation. Using DRUM with NEX-GDDP-CMIP6 dataset, we use the 50-year flood from historical scenario (1950–2014) as a threshold to evaluate future flood risk. Analysis of the return period changes (Δ Return period) for floods of this magnitude in future scenario (2015–2100) shows that negative Δ Return period indicates increased flood frequency and thus higher risk. Fig. 6 reveals distinct spatial heterogeneity in future flood risks across the CONUS, with consistent patterns across emission scenarios (SSP126, SSP245, SSP370, and SSP585). As scenarios intensify from SSP126 to SSP585, the proportion of basins experiencing increased flood risk rises from 47.8% to 57.1%. The widespread risk increase — affecting nearly half of the regions even under SSP126 — underscores climate change’s substantial impact on regional hydrology. Regional analysis shows contrasting patterns: flood risk

decreases in the Midwest and Northeast (including the Great Lakes region) but intensifies along the West Coast (particularly California) and Southeast regions (notably Florida). For high-risk regions under SSP585, evaluating flood early warning potential with perfect precipitation forecasts reveals promising results: 80.3% of basins could achieve at least 3-day ahead warnings, reaching beyond 5 days in the East and Pacific Northwest (Supplementary Fig. S4). With precipitation forecast accuracy being the key limitation, the rapid advancement of large models and big data in weather forecasting^{42,43,44} suggests an optimistic outlook for flood early warning capabilities in these vulnerable regions.

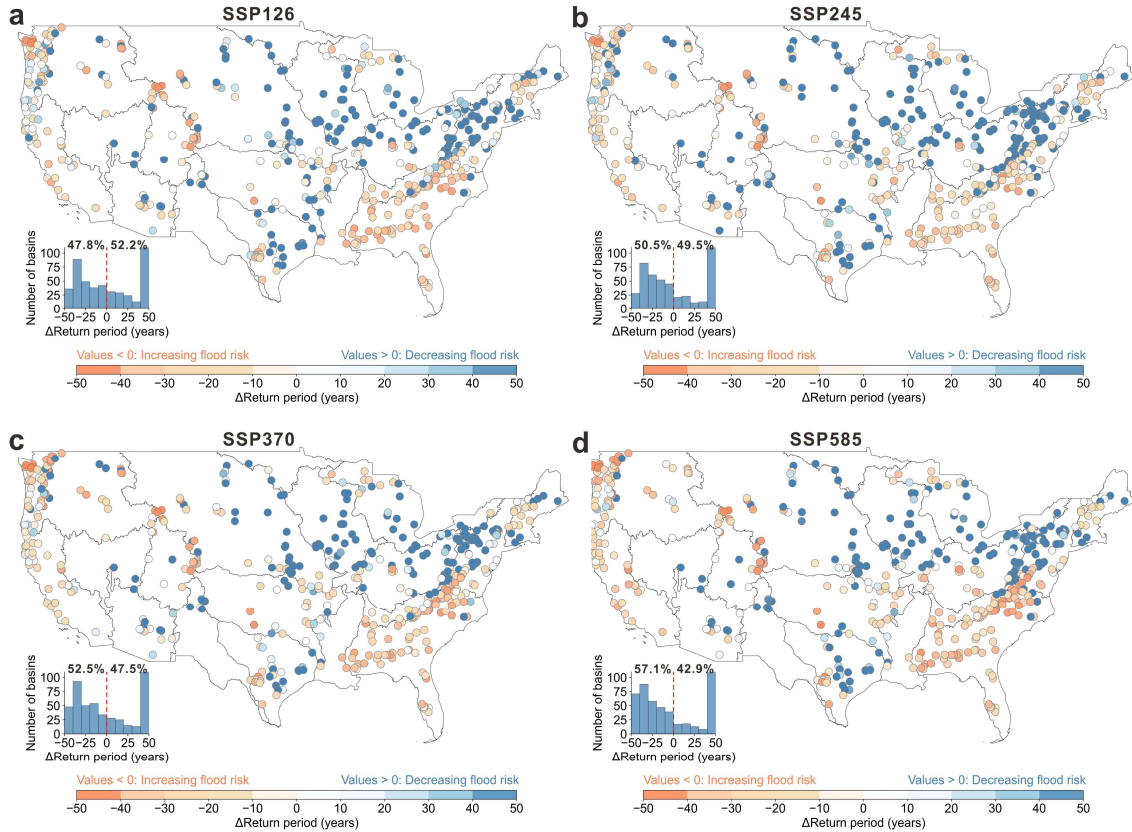


Fig. 6. Spatial distribution of flood risk under different emission scenarios. a,b,c,d, Changes in the return period (Δ Return period) of historical 50-year floods during future scenario under SSP126 (a), SSP245 (b), SSP370 (c), and SSP585 (d). Blue and orange dots indicate decreasing and increasing flood risk, respectively (Δ Return period > 0 and < 0). Histograms show the distribution of Δ Return period across all basins.

5. On the effectiveness of DRUM

We have shown the effectiveness of the DRUM over state-of-the-art deep learning methods for streamflow forecast, particularly for flood cases and uncertainty quantification. Here, we attribute DRUM's superior performance to three key aspects: distribution-free probabilistic modeling, multi-scale pattern decomposition, and flexible conditional generation. These elements work in concert to overcome fundamental limitations of traditional approaches.

Existing data-driven models rely on explicit probability distributions (e.g., Gaussian or

asymmetric Laplace) to characterize hydrological uncertainty. This parametric approach imposes rigid assumptions that fail to capture the complex, often heavy-tailed nature of flood distributions. DRUM eliminates these constraints through its diffusion framework, which implicitly learns the true data distribution through iterative denoising. The effectiveness of this distribution-free approach is demonstrated in Fig. 7a, where the learned cumulative distribution functions (CDFs) closely match the empirical distributions across all 531 basins. The model achieves particularly strong performance in capturing the distributional tails, with CDF differences (Δ CDF) showing minimal bias across the full range of normalized streamflow values (Fig. 7b). This flexibility proves particularly valuable in flood forecasting, where traditional parametric distributions often underestimate tail risks.

DRUM's iterative refinement process naturally decomposes the complex task of flood prediction into a hierarchy of more manageable sub-problems. The forward process progressively adds noise to the data, while the reverse process learns to reconstruct hydrological patterns at multiple temporal scales. This hierarchical decomposition is evident in the basin-specific CDFs shown in Fig. 7c, where DRUM successfully captures distinct distributional characteristics across diverse hydroclimatic gradients, from arid to humid regions. Early denoising steps recover broad seasonal and inter-annual patterns, while intermediate steps reconstruct medium-term weather responses. Final steps focus on capturing high-frequency dynamics and extreme events. This hierarchical approach enables more robust learning compared to LSTM models, which must simultaneously capture all temporal scales in a single prediction step.

DRUM advances hydrological modeling through its novel approach to incorporating meteorological conditions. While LSTM-based models embed conditioning information directly with fixed weights, DRUM employs a unique weighted combination of conditional and unconditional generation. The unconditional component captures the general empirical distribution of runoff sequences, as evidenced by the high-fidelity distribution matching in Fig. 7a-c, while the conditional component incorporates specific meteorological and catchment influences. The weighting mechanism, guided by classifier-free guidance²⁷, enables precise control over the relative influence of each component. This architecture allows DRUM to generate diverse yet physically consistent scenarios, maintain prediction accuracy while quantifying uncertainty, and adapt the strength of meteorological conditioning based on forecast confidence.

The effectiveness of this design is particularly evident in extreme event prediction, where DRUM achieves more accurate peak flow estimates with a 72.3% improvement in probabilistic skill, better calibrated uncertainty bounds as shown by comprehensive empirical evaluation and enhanced early warning capabilities demonstrated by lead time analysis. These architectural innovations combine to create a system that fundamentally advances the state of the art in flood forecasting. The distribution-free approach ensures flexibility, the multi-scale decomposition provides robustness, and the flexible conditioning enables precise control over meteorological influences. This combination proves particularly powerful for extreme event prediction, where traditional approaches often fall short.

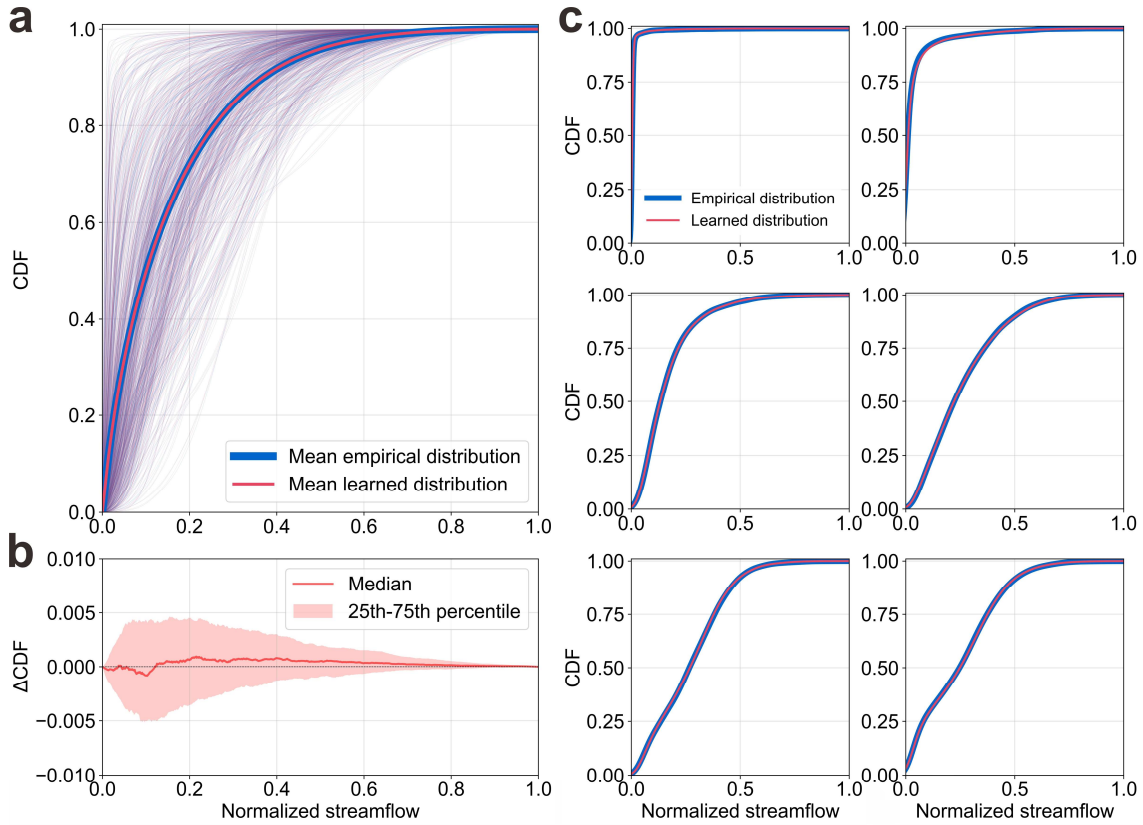


Fig. 7. Empirical runoff distribution reconstruction based on unconditional diffusion model across 531 studied basins. **a**, CDFs comparison between model-generated (learned) and observed (empirical) streamflow, with thin lines showing individual basins and thick lines representing their means. **b**, CDF differences ($\Delta\text{CDF} = \text{Learned} - \text{Empirical}$) showing median and interquartile range (25th–75th percentile) across normalized streamflow values. **c**, CDFs from six representative basins across hydroclimatic gradients (arid to humid), comparing theoretical and learned distributions. Streamflow data are log-transformed and min-max normalized per basin for visualization.

6. Discussion

The effectiveness of diffusion models is demonstrated in operational flood forecasting with precipitation forecasts as conditioning signals. As shown by comprehensive evaluations across different flood magnitudes and lead times (Fig. 3, Fig. 4), the diffusion process more effectively preserves and utilizes precipitation signals throughout generation. This fundamental advantage enables DRUM to consistently outperform LSTM-based models in flood prediction, particularly for extreme events, under both perfect and operational conditions. The success of precipitation conditioning points to opportunities for enhancement through additional hydrological signals. Although precipitation is the primary driver of floods, flood generation is modulated by multiple interacting factors^{34,35}, such as temperature governing snowmelt processes in cold regions³⁶ and soil moisture conditions influencing the rainfall-runoff relationship³⁷. Given the demonstrated strength in utilizing conditioning signals, diffusion models hold great promise in leveraging multiple signals to further improve extreme flood forecasting.

The spatial distribution of future flood risk revealed by DRUM reflects distinct flood generation mechanisms across the CONUS. The heightened risk in Western coastal and Southeastern regions aligns with their precipitation-driven flooding regime^{38,39,40}, corroborating projections of intensified precipitation-driven floods under climate change⁴¹. Nearly half of basins (47.8%) face increased flood risk even under the optimistic SSP126 scenario underscores the inevitability of certain climate impacts. Looking forward, we encourage a new generation of flood forecasting that harnesses both the unprecedented water surface observations from the Surface Water and Ocean Topography (SWOT) satellite and AI-enhanced weather prediction^{42,43,44}. This technological convergence, particularly through generative models that reveal both processes and their uncertainties, enables a transition toward systems with high spatial and temporal resolution. Such advances not only enhance fine-grid flood forecasting but also provide critical feedback to climate processes, bridging local hydrology and global dynamics for resilient water management.

7. Methods

DRUM

DRUM is a conditional diffusion model that generates T-day probabilistic runoff forecasts \mathbf{X} by incorporating three key components: t-day historical meteorological conditions \mathbf{H} , T-day precipitation forecasts \mathbf{F} , and static catchment attributes \mathbf{S} . The probabilistic forecasting process can be formulated as:

$$\hat{x}_{t+1}, \dots, \hat{x}_{t+T} \sim P_{\theta}(\mathbf{X}_{t+1:t+T} | \mathbf{H}_{1:t}, \mathbf{F}_{t+1:t+T}, \mathbf{S}), \quad (1)$$

where θ represents the model parameters, and $\hat{x}_{t+1}, \dots, \hat{x}_{t+T}$ are samples drawn from the conditional probability distribution P_{θ} .

To build a regional model, we first develop an unconditional diffusion model that incorporates basin's static attributes \mathbf{S} :

$$P_{\theta}(\mathbf{X}_{t+1:t+T} | \mathbf{S}) = \int p_r(\mathbf{X}_{t+1:t+T} | z) p_{\theta}(z | \mathbf{S}) dz, \quad (2)$$

where z represents the Gaussian noise variable, p_r represents the learned reverse process, and p_{θ} characterizes the noise-space transformation. Although termed “unconditional” as it excludes time-varying meteorological inputs (\mathbf{H} and \mathbf{F}), this base model necessarily conditions on \mathbf{S} since basin attributes fundamentally determine the runoff generation process, enabling a single model to capture diverse rainfall-runoff relationships across different catchments.

Building upon this proven framework, we extend DRUM to a conditional diffusion model by incorporating meteorological conditions:

$$P_{\theta}(\mathbf{X}_{t+1:t+T} | \mathbf{H}_{1:t}, \mathbf{F}_{t+1:t+T}, \mathbf{S}) = \int p_r(\mathbf{X}_{t+1:t+T} | z) p_{\theta}(z | \mathbf{H}_{1:t}, \mathbf{F}_{t+1:t+T}, \mathbf{S}) dz, \quad (3)$$

Then, we use classifier-free guidance approach to control how much the model relies on

conditional information. We introduce a weight w and form a linear combination of the conditional and unconditional predictions:

$$\tilde{P}_\theta = (1 + w) \cdot P_\theta(\mathbf{X}_{t+1:t+T} | \mathbf{H}_{1:t}, \mathbf{F}_{t+1:t+T}, \mathbf{S}) - w \cdot P_\theta(\mathbf{X}_{t+1:t+T} | \mathbf{S}). \quad (4)$$

When $w = 0$, the model is fully conditional, using the provided meteorological and hydrological inputs. As w increases, the model places even greater emphasis on these conditions, producing forecasts that more strongly reflect the given scenarios.

The diffusion framework establishes a bijective mapping between simple Gaussian distributions and complex runoff distributions through a forward-backward process. The forward process follows a Markov chain that progressively injects Gaussian noise into runoff, while the learned reverse process reconstructs samples through iterative denoising. In this framework, runoff data x_0 sampled from the true distribution $q(x_0)$ is gradually transformed into Gaussian noise x_T through T diffusion steps. The forward process can be defined as:

$$q(x_t | x_{t-1}) = N\left(x_t; \sqrt{(1 - \beta_t)}x_{t-1}, \beta_t \mathbf{I}\right), \quad (5)$$

where β_t is a predefined variance schedule that controls the noise level at each step, and the time step t progresses from 1 to T .

The reverse process $p(x_{t-1} | x_t)$ reconstructs the runoff distribution by iteratively denoising samples from a standard normal distribution $N(0,1)$. This process is modeled as a learnable Markov chain where each step gradually denoises the data through a neural network that learns the transition dynamics. Given the conditional information y , the reverse transition can be formulated as:

$$p_\theta(x_{t-1} | x_t, y) = N\left(x_{t-1}; \mu_\theta(x_t, t, y), \sigma_\theta^2(x_t, t, y) \mathbf{I}\right), \quad (6)$$

where μ_θ and σ_θ^2 are learned functions parameterized by θ . Upon optimization of $p_\theta(x_{t-1} | x_t, y)$, we can generate future runoff sequences from Gaussian noise x_T given conditional information y .

Detailed derivations of DRUM are provided in Supplementary Text 1.

Datasets

The CAMELS dataset comprises 671 basins across the CONUS, encompassing diverse geological, ecological, and climatic conditions. The dataset provides daily meteorological forcings (1980–2010) from three gridded products: Daymet (0.01°), Maurer (0.125°), and NLDAS (0.125°). We utilize five forcing variables including precipitation (mm day⁻¹), maximum and minimum temperature (°C), shortwave radiation (W m⁻²), and vapor pressure (Pa). CAMELS also contains 27 static catchment attributes (Supplementary Table S1), along with daily streamflow observations from the United States Geological Survey (USGS). Following Klotz et al.²⁵, we select 531 basins with areas ranging from 4 to 2000 km², excluding larger basins and those showing significant area calculation discrepancies (>10%).

The ECMWF-IFS reforecast dataset provides precipitation forecasts at 0.125° spatial

resolution, which is generated twice weekly within a 20-year rolling window. Each forecast consists of four perturbed ensemble members with 6-hourly accumulations extending to 7 days ahead. We utilize reforecasts from 30 September 1995 to 1 October 2005, aggregating 6-hourly data into daily total precipitation. Approximately 10% of missing data are filled using ERA5-Land reanalysis (0.1° resolution). All gridded data are area-weighted to obtain basin-scale estimates.

The NEX-GDDP-CMIP6 dataset provides high-resolution (0.25°) climate projections. We utilize daily data from five GCMs (CanESM5, CESM2, CNRM-CM6-1, EC-Earth3, and MPI-ESM1-2-HR) spanning historical (1950–2014) and future periods (2015–2100) under four scenarios (SSP126, SSP245, SSP370, and SSP585). The variables include precipitation, mean temperature, maximum and minimum temperature, shortwave radiation, and relative humidity (Supplementary Table S2). To maintain consistency with CAMELS meteorological forcings, we derive vapor pressure from mean temperature and relative humidity and apply Distribution Mapping to correct systematic biases against Daymet data during 1980–2014, as Daymet provides the highest spatial resolution (0.01°) among the three observation-driven products (detailed procedures in Supplementary Text 2). All bias-corrected outputs are area-weighted to basin scale, and multi-model means are calculated by equal weighting.

Modeling frameworks

We compare DRUM with two LSTM-based baseline models: a deterministic model (LSTM-d) and a probabilistic model (LSTM-p). All models share a similar backbone architecture, comprising an encoder-decoder LSTM with static catchment attribute embedding components. The models take as input 365-day historical meteorological forcing sequences, 27 static catchment attributes, and T-day precipitation forecasts to generate T-day runoff predictions.

The key distinction lies in their modeling frameworks. DRUM leverages a diffusion process for probabilistic forecasting, LSTM-d produces deterministic forecasts optimized with NSE* loss function¹⁵, while LSTM-p characterizes uncertainty through a single asymmetric Laplace distribution¹⁰, outputting location (μ), scale (σ), and skewness (τ) parameters at each forecast step. Detailed model architectures and training configurations are presented in Supplementary Table S3.

Experimental setup

We design three experiments to evaluate the proposed DRUM against the LSTM baselines, focusing on nowcasting, operational forecasting, and future flood risk assessment, respectively.

In Experiment 1, we evaluate single-step streamflow nowcasting (0-day lead time) utilizing merged meteorological forcings from three sources (Daymet, Maurer, and NLDAS) in the CAMELS dataset, which has demonstrated optimal performance⁴⁶. The input features comprise precipitation (Prep), maximum temperature (Tmax), minimum temperature (Tmin), shortwave radiation (Srad), and vapor pressure (Vp), along with daily streamflow observations from USGS. Following Klotz et al.²⁵, we split the dataset

into training (1 October 1980–30 September 1990), validation (1 October 1990–30 September 1995), and testing periods (1 October 1995–1 September 2005).

Experiment 2 extends to operational forecasting with future precipitation forecasts. We generate 7-dimensional output sequences (1–7-day lead times), utilizing Daymet data for the same meteorological features as Experiment 1. During training, we employ Daymet precipitation observations as perfect forecasts. For testing, we evaluate models with both perfect forecasts (Daymet observations) and ECMWF-IFS reforecasts to isolate the impacts from precipitation forecasts and rainfall-runoff modeling. The data split remains consistent with Experiment 1.

Experiment 3 addresses on future flood risk assessment. We adopt the nowcasting setup and model configurations from Experiment 1, training the models with Daymet data and driving them with NEX-GDDP-CMIP6 climate projections. These projections span both historical (1950–2014) and future periods (2015–2100) under four Shared Socioeconomic Pathway scenarios (SSP126, SSP245, SSP370, SSP585).

The probabilistic models (DRUM and LSTM-p) generate 50 ensemble forecasts per time step to characterize prediction uncertainty, whereas the deterministic model (LSTM-d) produces single-valued outputs. Model evaluation compares predictions against observations, using all ensemble members for the probabilistic metric and ensemble means for deterministic metrics.

All experiments are conducted on a single NVIDIA RTX 4090 GPU. The training process requires 13.5, 2.5, and 4.8 hours for DRUM, LSTM-p, and LSTM-d, respectively. For 531 basins with 10-year test data, DRUM requires 90 hours to generate 50 samples at each time step, while the sampling time for both LSTM variants is negligible. DRUM's sampling efficiency could potentially be improved by 20–50 times through the Denoising Diffusion Implicit Models⁴⁷ acceleration strategy.

Probabilistic metric

Continuous Ranked Probability Score (CRPS)⁴⁸ is used to evaluate probabilistic forecasts, measuring both calibration and sharpness of the forecast distributions. For deterministic forecasts, CRPS reduces to Mean Absolute Error (MAE), which enables direct comparison across different approaches, with values ranging from 0 (perfect forecast) to infinity.

Deterministic metrics

Multiple metrics are used to assess model performance, with probabilistic forecasts evaluated using ensemble means. The overall skill is measured by Kling-Gupta Efficiency (KGE), Nash-Sutcliffe Efficiency (NSE), MAE, and their components (α -NSE, β -NSE, COR). Flow-specific performance is evaluated using three flow-duration-curve-based metrics⁴⁹: high-segment volume bias (FHV) for the top 1% of flows, low-segment volume bias (FLV) for flows below the 30th percentile, and midsegment slope bias (FMS) for flows between the 20th and 80th percentiles. Peak-Timing error (P-T) measures the temporal accuracy of peak flows.

Flood event detection metrics

We evaluate flood detection skill using precision, recall, and F1 score, with values ranging from 0 to 1 (1 indicating perfect performance). Flood magnitudes are defined using return periods following the USGS Bulletin 17B⁵⁰, where we fit the Log-Pearson Type III distribution to annual maximum daily streamflow series for each basin. A flood event is considered correctly forecast when both observed and forecasted peak flows occur within the same natural day and exceed the flow threshold corresponding to the specified return period. Precision quantifies the proportion of true floods among all predicted flood events, while recall measures the fraction of actual flood events that were successfully identified. The F1 score, calculated as the harmonic mean of precision and recall, provides a balanced assessment of detection skill.

Early warning metric

We quantify the early warning skill using mean lead time. For each flood event, we determine the maximum lead time (in days) at which the forecast successfully detects the flood, with unsuccessful forecasts assigned zero lead time. The basin-specific warning skill is then represented by the mean lead time across all flood events within that basin.

Detailed formulations and mathematical definitions of all evaluation metrics are presented in Supplementary Text 3.

Reference

1. Doocy, S., Daniels, A., Murray, S., & Kirsch, T. D. (2013). The human impact of floods: a historical review of events 1980-2009 and systematic literature review. *PLoS currents*, 5.
2. United Nations Office for Disaster Risk Reduction. (2020). The human cost of disasters: An overview of the last 20 years (2000-2019). UNDRR.
3. Milly, P. C. D., Wetherald, R. T., Dunne, K. A., & Delworth, T. L. (2002). Increasing risk of great floods in a changing climate. *Nature*, 415(6871), 514-517.
4. Yin, J., Gentine, P., Zhou, S., Sullivan, S. C., Wang, R., Zhang, Y., & Guo, S. (2018). Large increase in global storm runoff extremes driven by climate and anthropogenic changes. *Nature communications*, 9(1), 4389.
5. Rentschler, J., Avner, P., Marconcini, M., Su, R., Strano, E., Vousdoukas, M., & Hallegatte, S. (2023). Global evidence of rapid urban growth in flood zones since 1985. *Nature*, 622(7981), 87-92.
6. Feng, D., Beck, H., de Bruijn, J., Sahu, R. K., Satoh, Y., Wada, Y., ... & Shen, C. (2023). Deep dive into global hydrologic simulations: Harnessing the power of deep learning and physics-informed differentiable models (δ HBV-globe1. 0-hydroDL). *Geoscientific Model Development Discussions*, 2023, 1-23.
7. Bárdossy, A., & Anwar, F. (2022). Why our rainfall-runoff models keep underestimating the peak flows?. *Hydrology and Earth System Sciences Discussions*, 2022, 1-30.
8. Jain, S. K., Mani, P., Jain, S. K., Prakash, P., Singh, V. P., Tullos, D., ... & Dimri, A. P. (2018). A Brief review of flood forecasting techniques and their applications. *International journal of river basin management*, 16(3), 329-344.
9. Auer, A., Gauch, M., Kratzert, F., Nearing, G., Hochreiter, S., & Klotz, D. (2024). A data-centric perspective on the information needed for hydrological uncertainty predictions. *Hydrology and Earth System Sciences Discussions*, 2024, 1-37.
10. Nearing, G., Cohen, D., Dube, V., Gauch, M., Gilon, O., Harrigan, S., ... & Matias, Y. (2024). Global prediction of extreme floods in ungauged watersheds. *Nature*, 627(8004), 559-563.
11. Frame, J. M., Kratzert, F., Klotz, D., Gauch, M., Shalev, G., Gilon, O., ... & Nearing, G. S. (2022). Deep learning rainfall-runoff predictions of extreme events. *Hydrology and Earth System Sciences*, 26(13), 3377-3392.
12. Cui, Z., Guo, S., Chen, H., Liu, D., Zhou, Y., & Xu, C. Y. (2024). Quantifying and reducing flood forecast uncertainty by the CHUP-BMA method. *Hydrology and Earth System Sciences*, 28(13), 2809-2829.
13. Zhang, B., Ouyang, C., Cui, P., Xu, Q., Wang, D., Zhang, F., ... & Zhang, Q. (2024). Deep learning for cross-region streamflow and flood forecasting at a global scale. *The Innovation*, 5(3).
14. Kratzert, F., Klotz, D., Brenner, C., Schulz, K., & Herrnegger, M. (2018). Rainfall-runoff modelling using long short-term memory (LSTM) networks. *Hydrology and Earth System Sciences*, 22(11), 6005-6022.

15. Kratzert, F., Klotz, D., Shalev, G., Klambauer, G., Hochreiter, S., & Nearing, G. (2019). Towards learning universal, regional, and local hydrological behaviors via machine learning applied to large-sample datasets. *Hydrology and Earth System Sciences*, 23(12), 5089-5110.
16. Feng, D., Fang, K., & Shen, C. (2020). Enhancing streamflow forecast and extracting insights using long-short term memory networks with data integration at continental scales. *Water Resources Research*, 56(9), e2019WR026793.
17. Feng, D., Beck, H., Lawson, K., & Shen, C. (2023). The suitability of differentiable, physics-informed machine learning hydrologic models for ungauged regions and climate change impact assessment. *Hydrology and Earth System Sciences*, 27(12), 2357-2373.
18. De la Fuente, L. A., Ehsani, M. R., Gupta, H. V., & Condon, L. E. (2023). Towards interpretable LSTM-based modelling of hydrological systems. *Hydrology and Earth System Sciences Discussions*, 2023, 1-36.
19. Nai, C., Liu, X., Tang, Q., Liu, L., Sun, S., & Gaffney, P. P. (2024). A novel strategy for automatic selection of cross-basin data to improve local machine learning-based runoff models. *Water Resources Research*, 60(5), e2023WR035051.
20. Troin, M., Arsenault, R., Wood, A. W., Brissette, F., & Martel, J. L. (2021). Generating ensemble streamflow forecasts: A review of methods and approaches over the past 40 years.
21. Krzysztofowicz, R. (1999). Bayesian theory of probabilistic forecasting via deterministic hydrologic model. *Water Resources Research*, 35(9), 2739-2750.
22. Han, S., & Coulibaly, P. (2017). Bayesian flood forecasting methods: A review. *Journal of Hydrology*, 551, 340-351.
23. Beven, K., & Binley, A. (1992). The future of distributed models: model calibration and uncertainty prediction. *Hydrological processes*, 6(3), 279-298.
24. Beven, K., & Binley, A. (2014). GLUE: 20 years on. *Hydrological processes*, 28(24), 5897-5918.
25. Klotz, D., Kratzert, F., Gauch, M., Keefe Sampson, A., Brandstetter, J., Klambauer, G., ... & Nearing, G. (2022). Uncertainty estimation with deep learning for rainfall-runoff modeling. *Hydrology and Earth System Sciences*, 26(6), 1673-1693.
26. Ho, J., Jain, A., & Abbeel, P. (2020). Denoising diffusion probabilistic models. *Advances in neural information processing systems*, 33, 6840-6851.
27. Ho, J., & Salimans, T. (2022). Classifier-free diffusion guidance. *arXiv preprint arXiv:2207.12598*.
28. Dieleman, S. (2023, July 20). *Perspectives on diffusion*. *Sander.ai*. <https://sander.ai/2023/07/20/perspectives.html>.
29. Newman, A. J., Clark, M. P., Sampson, K., Wood, A., Hay, L. E., Bock, A., ... & Duan, Q. (2015). Development of a large-sample watershed-scale hydrometeorological data set for the contiguous USA: data set characteristics and assessment of regional variability in hydrologic model performance. *Hydrology and Earth System Sciences*, 19(1), 209-223.
30. Addor, N., Newman, A. J., Mizukami, N., & Clark, M. P. (2017). The CAMELS data set: catchment attributes and meteorology for large-sample studies. *Hydrology and*

- Earth System Sciences*, 21(10), 5293-5313.
31. Thrasher, B., Wang, W., Michaelis, A., Melton, F., Lee, T., & Nemani, R. (2022). NASA global daily downscaled projections, CMIP6. *Scientific data*, 9(1), 262.
 32. Rombach, R., Blattmann, A., Lorenz, D., Esser, P., & Ommer, B. (2022). High-resolution image synthesis with latent diffusion models. In *Proceedings of the IEEE/CVF conference on computer vision and pattern recognition* (pp. 10684-10695).
 33. Hooeboom, E., Nielsen, D., Jaini, P., Forré, P., & Welling, M. (2021). Argmax flows and multinomial diffusion: Learning categorical distributions. *Advances in Neural Information Processing Systems*, 34, 12454-12465.
 34. Jiang, S., Tarasova, L., Yu, G., & Zscheischler, J. (2024). Compounding effects in flood drivers challenge estimates of extreme river floods. *Science Advances*, 10(13), ead14005.
 35. Bertola, M., Viglione, A., Vorogushyn, S., Lun, D., Merz, B., & Blöschl, G. (2021). Do small and large floods have the same drivers of change? A regional attribution analysis in Europe. *Hydrology and Earth System Sciences*, 25(3), 1347-1364.
 36. Blöschl, G., Hall, J., Viglione, A., Perdigão, R. A., Parajka, J., Merz, B., ... & Živković, N. (2019). Changing climate both increases and decreases European river floods. *Nature*, 573(7772), 108-111.
 37. Wasko, C., & Nathan, R. (2019). Influence of changes in rainfall and soil moisture on trends in flooding. *Journal of Hydrology*, 575, 432-441.
 38. Berghuijs, W. R., Woods, R. A., Hutton, C. J., & Sivapalan, M. (2016). Dominant flood generating mechanisms across the United States. *Geophysical Research Letters*, 43(9), 4382-4390.
 39. Jiang, S., Zheng, Y., Wang, C., & Babovic, V. (2022). Uncovering flooding mechanisms across the contiguous United States through interpretive deep learning on representative catchments. *Water Resources Research*, 58(1), e2021WR030185.
 40. Stein, L., Clark, M. P., Knoben, W. J., Pianosi, F., & Woods, R. A. (2021). How do climate and catchment attributes influence flood generating processes? A large-sample study for 671 catchments across the contiguous USA. *Water Resources Research*, 57(4), e2020WR028300.
 41. Zhang, S., Zhou, L., Zhang, L., Yang, Y., Wei, Z., Zhou, S., ... & Dai, Y. (2022). Reconciling disagreement on global river flood changes in a warming climate. *Nature Climate Change*, 12(12), 1160-1167.
 42. Ravuri, S., Lenc, K., Willson, M., Kangin, D., Lam, R., Mirowski, P., ... & Mohamed, S. (2021). Skilful precipitation nowcasting using deep generative models of radar. *Nature*, 597(7878), 672-677.
 43. Zhang, Y., Long, M., Chen, K., Xing, L., Jin, R., Jordan, M. I., & Wang, J. (2023). Skilful nowcasting of extreme precipitation with NowcastNet. *Nature*, 619(7970), 526-532.
 44. Price, I., Sanchez-Gonzalez, A., Alet, F. et al. Probabilistic weather forecasting with machine learning. *Nature* (2024).
 45. Radford, A., Kim, J. W., Hallacy, C., Ramesh, A., Goh, G., Agarwal, S., ... & Sutskever, I. (2021, July). Learning transferable visual models from natural language supervision. In *International conference on machine learning* (pp. 8748-8763).

PMLR.

46. Kratzert, F., Klotz, D., Hochreiter, S., & Nearing, G. S. (2021). A note on leveraging synergy in multiple meteorological data sets with deep learning for rainfall–runoff modeling. *Hydrology and Earth System Sciences*, 25(5), 2685-2703.
47. Song, J., Meng, C., & Ermon, S. (2020). Denoising diffusion implicit models. *arXiv preprint arXiv:2010.02502*.
48. Gneiting, T., & Raftery, A. E. (2007). Strictly proper scoring rules, prediction, and estimation. *Journal of the American statistical Association*, 102(477), 359-378.
49. Yilmaz, K. K., Gupta, H. V., & Wagener, T. (2008). A process-based diagnostic approach to model evaluation: Application to the NWS distributed hydrologic model. *Water resources research*, 44(9).
50. Interagency Advisory Committee on Water Data. Guidelines for Determining Flood Flow Frequency Bulletin #17B of the Hydrology Subcommittee (US Department of the Interior Geological Survey, 1982).

Supplementary Information

Supplementary Text 1. Diffusion-based runoff model.

Supplementary Text 2. Methodology for vapor pressure derivation and bias correction of CMIP6 daily variables using Distribution Mapping.

Supplementary Text 3. Evaluation metrics.

Supplementary Fig. S1. Probabilistic forecasting skill comparison between DRUM and LSTM-d.

Supplementary Fig. S2. Relationships between uncertainty and meteorological forcings in probabilistic models.

Supplementary Fig. S3. Distribution of regression slopes between observed and forecasted precipitation across 531 representative basins.

Supplementary Fig. S4. Flood warning capabilities in high-risk basins under climate change.

Supplementary Fig. S5. Temporal evolution of key meteorological variables under different SSP scenarios from 1950 to 2100.

Supplementary Table S1. Comprehensive overview of CAMELS static catchment attributes.

Supplementary Table S2. Data availability of daily meteorological variables across CMIP6 GCMs under different scenarios.

Supplementary Table S3. Configurations of model architectures and training settings.

Supplementary Text 1. Diffusion-based runoff model.

Diffusion models overview

Diffusion models represent a class of generative models that leverage the underlying principles of diffusion processes to transform Gaussian noise into target data distributions for sample generation. These models are based on a forward-backward process, where the forward process gradually adds noise to data, and the reverse process learns to remove the noise to recover the original data. The key idea behind diffusion models is to parameterize the reverse process to model the data generation process effectively. When applied to runoff forecasting, these models provide an innovative framework for capturing the intricate dynamics and inherent uncertainties within hydrological systems.

In the forward process, data x_0 represents a sample from the runoff distribution $q(x_0)$, and x_0 is gradually transformed into a pure noise Gaussian sequence x_T through a series of diffusion steps T . The forward process can be defined as:

$$q(x_t|x_{t-1}) = N\left(x_t; \sqrt{(1-\beta_t)}x_{t-1}, \beta_t \mathbf{I}\right), \quad (\text{S1})$$

where β_t is a predefined variance schedule, and the time step t progresses from 1 to T .

Given $\alpha_t = 1 - \beta_t$, $\bar{\alpha}_t = \prod_{i=1}^t \alpha_i$, and ϵ_t is Gaussian noise drawn from a standard normal distribution $N(0,1)$, we can express this relationship in a more direct form as:

$$\begin{aligned} x_t &= \sqrt{1-\beta_t}x_{t-1} + \sqrt{\beta_t}\epsilon_{t-1} \\ &= \sqrt{\alpha_t}(\sqrt{\alpha_{t-1}}x_{t-2} + \sqrt{1-\alpha_{t-1}}\epsilon_{t-2}) + \sqrt{1-\alpha_t}\epsilon_{t-1} \\ &= \sqrt{\alpha_t\alpha_{t-1}}x_{t-2} + \sqrt{\alpha_t - \alpha_t\alpha_{t-1}}\epsilon_{t-2} + \sqrt{1-\alpha_t}\epsilon_{t-1} \\ &= \sqrt{\alpha_t\alpha_{t-1}}x_{t-2} + \sqrt{1-\alpha_t\alpha_{t-1}}\bar{\epsilon}_{t-2} \\ &= \dots \\ &= \sqrt{\prod_{i=1}^t \alpha_i} x_0 + \sqrt{1-\prod_{i=1}^t \alpha_i} \bar{\epsilon}_0 \\ &= \sqrt{\bar{\alpha}_t} X_0 + \sqrt{1-\bar{\alpha}_t} \bar{\epsilon}_0. \end{aligned} \quad (\text{S2})$$

In Equation (S2), we exploit a fundamental property of Gaussian distributions: the sum of two independent Gaussian random variables yields another Gaussian distribution, whose mean equals the sum of the individual means and whose variance is the sum of the individual variances. Consequently, x_t can be sampled directly from x_0 , with this stochastic process expressed in closed form as:

$$q(x_t|x_0) = N\left(x_t; \sqrt{\bar{\alpha}_t}x_0, (1-\bar{\alpha}_t)\mathbf{I}\right). \quad (\text{S3})$$

Given x_0 and a Gaussian noise ϵ , and applying the transformation:

$$x_t = \sqrt{\bar{\alpha}_t}x_0 + \sqrt{1-\bar{\alpha}_t}\epsilon. \quad (\text{S4})$$

When $t \rightarrow T$, $\beta_t \rightarrow 1$, consequently $\bar{\alpha}_T \rightarrow 0$, and x_T closely approximates a Gaussian distribution. During the forward process, noise is progressively incorporated until the data's spatial structure dissipates, resulting in pure noise.

The reverse process $p(x_{t-1}|x_t)$, aims to reverse the noising process, gradually

transforming the noisy data x_t from $N(0,1)$ and employ a sequence of neural networks to systematically remove noise, generating the sequence $x_t \rightarrow x_0$. This framework suggests modeling the reverse process as a learnable Markov chain:

$$p_\theta(x_{t-1}|x_t) = N(x_{t-1}; \mu_\theta(x_t, t), \sigma_\theta^2(x_t, t)I), \quad (S5)$$

where μ_θ and σ_θ^2 are learned functions parameterized by θ .

The model parameters θ are optimized by maximizing the variational lower bound (VLB) of the data log-likelihood. The learned model closely approximates the true reverse diffusion process while maintaining computational feasibility. The VLB optimization can be formally expressed as:

$$\begin{aligned} \mathbb{E}_{q(x_0)}(-\log p_\theta(x_0)) &\leq \mathbb{E}_{q(x_0)}[-\log p_\theta(x_0) + D_{KL}(q(x_{1:T}|x_0)||p_\theta(x_{1:T}|x_0))] \\ &= \mathbb{E}_{q(x_0)} \left[-\log p_\theta(x_0) + \int q(x_{1:T}|x_0) \log \frac{q(x_{1:T}|x_0)}{p_\theta(x_{0:T})/p_\theta(x_0)} dx_{1:T} \right] \\ &= \mathbb{E}_{q(x_0)} \left[-\log p_\theta(x_0) + \int q(x_{1:T}|x_0) \log \frac{q(x_{1:T}|x_0)}{p_\theta(x_{0:T})} dx_{1:T} + \log p_\theta(x_0) \right] \\ &= \mathbb{E}_{q(x_{0:T})} \log \frac{q(x_{1:T}|x_0)}{p_\theta(x_{0:T})} = L_{VLB}. \end{aligned} \quad (S6)$$

To better understand the optimization objective and isolate the key components of the learning process, we can decompose and rewrite the VLB in a more mathematically tractable form as:

$$\begin{aligned} L_{VLB} &= \mathbb{E}_{q(x_{0:T})} \left[\log \frac{q(x_{1:T}|x_0)}{p_\theta(x_{0:T})} \right] \\ &= \mathbb{E}_q \left[\log \frac{\prod_{t=1}^T q(x_t|x_{t-1})}{p_\theta(x_T) \prod_{t=1}^T p_\theta(x_{t-1}|x_t)} \right] \\ &= \mathbb{E}_q \left[-\log p_\theta(x_T) + \sum_{t=1}^T \log \frac{q(x_t|x_{t-1})}{p_\theta(x_{t-1}|x_t)} \right] \\ &= \mathbb{E}_q \left[-\log p_\theta(x_T) + \sum_{t=2}^T \log \frac{q(x_t|x_{t-1})}{p_\theta(x_{t-1}|x_t)} + \log \frac{q(x_1|x_0)}{p_\theta(x_0|x_1)} \right] \\ &= \mathbb{E}_q \left[-\log p_\theta(x_T) + \sum_{t=2}^T \log \left(\frac{q(x_{t-1}|x_t, x_0)}{p_\theta(x_{t-1}|x_t)} \cdot \frac{q(x_t|x_0)}{q(x_{t-1}|x_0)} \right) + \log \frac{q(x_1|x_0)}{p_\theta(x_0|x_1)} \right] \\ &= \mathbb{E}_q \left[-\log p_\theta(x_T) + \sum_{t=2}^T \log \frac{q(x_{t-1}|x_t, x_0)}{p_\theta(x_{t-1}|x_t)} + \sum_{t=2}^T \log \frac{q(x_t|x_0)}{q(x_{t-1}|x_0)} + \log \frac{q(x_1|x_0)}{p_\theta(x_0|x_1)} \right] \\ &= \mathbb{E}_q \left[-\log p_\theta(x_T) + \sum_{t=2}^T \log \frac{q(x_{t-1}|x_t, x_0)}{p_\theta(x_{t-1}|x_t)} + \log \frac{q(x_T|x_0)}{q(x_1|x_0)} + \log \frac{q(x_1|x_0)}{p_\theta(x_0|x_1)} \right] \\ &= \mathbb{E}_q \left[\log \frac{q(x_T|x_0)}{p_\theta(x_T)} + \sum_{t=2}^T \log \frac{q(x_{t-1}|x_t, x_0)}{p_\theta(x_{t-1}|x_t)} - \log p_\theta(x_0|x_1) \right] \\ &= \mathbb{E}_q \left[D_{KL}(q(x_T|x_0)||p_\theta(x_T)) + \sum_{t=2}^T D_{KL}(q(x_{t-1}|x_t, x_0)||p_\theta(x_{t-1}|x_t)) - \log p_\theta(x_0|x_1) \right]. \end{aligned} \quad (S7)$$

This formulation yields an elegant interpretation when examining each constituent term:

- 1) The reconstruction term $L_0 = -\mathbb{E}_q[\log p_\theta(x_0|x_1)]$ quantifies how well the model reconstructs the original data.
- 2) The prior matching term $L_T = \mathbb{E}_q[D_{KL}(q(x_T|x_0)||p_\theta(x_T))]$ quantifies the distributional alignment between the fully noised input and the standard Gaussian

prior. This term vanishes under our assumptions, as the diffusion process ensures complete convergence to Gaussian noise at the terminal time step T .

- 3) The denoising matching term $L_t = D_{KL}(q(x_{t-1}|x_t, x_0)||p_\theta(x_{t-1}|x_t))$ is the core optimization objective. Here, $q(x_{t-1}|x_t, x_0)$ serves as the ground-truth signal while $p_\theta(x_{t-1}|x_t)$ represents our learned denoising transition. The optimization process minimizes the discrepancy between these two denoising steps.

When x_0 is known, $q(x_{t-1}|x_t, x_0)$ can be derived through Bayes' theorem, resulting in a Gaussian distribution:

$$\begin{aligned}
q(x_{t-1}|x_t, x_0) &= q(x_t|x_{t-1}, x_0) \frac{q(x_{t-1}|x_0)}{q(x_t|x_0)} \\
&\propto \exp\left(-\frac{1}{2}\left(\frac{(x_t - \sqrt{\alpha_t}x_{t-1})^2}{\beta_t} + \frac{(x_{t-1} - \sqrt{\bar{\alpha}_{t-1}}x_0)^2}{1 - \bar{\alpha}_{t-1}} - \frac{(x_t - \sqrt{\bar{\alpha}_t}x_0)^2}{1 - \bar{\alpha}_t}\right)\right) \\
&= \exp\left(-\frac{1}{2}\left(\frac{\alpha_t}{\beta_t} + \frac{1}{1 - \bar{\alpha}_{t-1}}\right)x_{t-1}^2 + \left(\frac{2\sqrt{\alpha_t}}{\beta_t}x_t + \frac{2\sqrt{\bar{\alpha}_{t-1}}}{1 - \bar{\alpha}_{t-1}}x_0\right)x_{t-1} + \mathcal{C}(x_t, x_0)\right) \\
&= N(x_{t-1}; \tilde{\mu}(x_t, x_0), \tilde{\beta}(t)I). \tag{S8}
\end{aligned}$$

Referring to the previously derived Gaussian forms in equations (S4) and (S8), we can express:

$$\tilde{\mu}(x_t, x_0) = \frac{1}{\sqrt{\bar{\alpha}_t}}\left(x_t - \frac{1 - \alpha_t}{\sqrt{1 - \bar{\alpha}_t}}\epsilon_\theta(x_t, t)\right). \tag{S9}$$

By examining $L_t = D_{KL}(q(x_{t-1}|x_t, x_0)||p_\theta(x_{t-1}|x_t))$ and leveraging the derivations from equations (S5), (S8) and (S9), we can formulate the loss function as:

$$\begin{aligned}
L_t &= \mathbb{E}_{x_0, \epsilon} \left[\frac{1}{2\|\Sigma_\theta(x_t, t)\|_2^2} \left\| \tilde{\mu}(x_t, x_0) - \mu_\theta(x_t, t) \right\|^2 \right] \\
&= \mathbb{E}_{x_0, \epsilon} \left[\frac{1}{2\|\Sigma_\theta\|_2^2} \left\| \frac{1}{\sqrt{\bar{\alpha}_t}} \left(x_t - \frac{1 - \alpha_t}{\sqrt{1 - \bar{\alpha}_t}} \epsilon_t \right) - \frac{1}{\sqrt{\bar{\alpha}_t}} \left(x_t - \frac{1 - \alpha_t}{\sqrt{1 - \bar{\alpha}_t}} \epsilon_\theta(x_t, t) \right) \right\|^2 \right] \\
&= \mathbb{E}_{x_0, \epsilon} \left[\frac{(1 - \alpha_t)^2}{2\alpha_t(1 - \bar{\alpha}_t)\|\Sigma_\theta\|_2^2} \left\| \epsilon_t - \epsilon_\theta(x_t, t) \right\|^2 \right] \\
&= \mathbb{E}_{x_0, \epsilon} \left[\frac{(1 - \alpha_t)^2}{2\alpha_t(1 - \bar{\alpha}_t)\|\Sigma_\theta\|_2^2} \left\| \epsilon_t - \epsilon_\theta \left(\sqrt{\bar{\alpha}_t}x_0 + \sqrt{1 - \bar{\alpha}_t}\epsilon_t, t \right) \right\|^2 \right]. \tag{S10}
\end{aligned}$$

Following Ho et al.⁰, we utilize their elegant formulation of a simplified loss function. Their derivation yields a streamlined objective L_{simple} that directly compares the model's predicted noise ϵ_θ and the actual noise ϵ :

$$L_{simple} = E_{x_0, \epsilon} \left[\left\| \epsilon - \epsilon_\theta \left(\sqrt{\bar{\alpha}_t}x_0 + \sqrt{1 - \bar{\alpha}_t}\epsilon, t \right) \right\|^2 \right], \tag{S11}$$

where, ϵ represents the noise added during the forward process, and ϵ_θ is the noise predicted by the model.

Conditional diffusion

In the context of runoff forecasting, we employ both unconditional and conditional diffusion models. The unconditional model captures the general empirical distribution of runoff sequences, whereas the conditional model refines predictions by incorporating additional contextual information, such as past meteorological conditions, static catchment attributes, and current weather states. These models are grounded in score-based diffusion techniques^{S2}, which utilize the gradient of the log probability density (score function). This score function, defined as $\nabla \log p(x)$, captures the geometric structure of the data distribution and enables sample generation without explicit density modeling.

The objective is to approximate the conditional distribution $p(x_t | y)$, where x_t represents the runoff sequence at time t , and y denotes the conditioning information. In diffusion models, noise prediction is modeled via ϵ_θ . For the conditional case, the noise is predicted as:

$$\epsilon_\theta(x_t, y) = -\nabla_{x_t} \log p(x_t | y), \quad (\text{S12})$$

while for the unconditional case, the noise prediction depends solely on x_t and is given by:

$$\epsilon_\theta(x_t) = -\nabla_{x_t} \log p(x_t). \quad (\text{S13})$$

To interpolate between the conditional and unconditional predictions, we apply the classifier-free guidance (CFG) method^{S3}. This approach introduces a guidance weight w that modifies the predicted noise as:

$$\epsilon_\theta(x_t, y)_{\text{CFG}} = (1 + w)\epsilon_\theta(x_t, y) - w\epsilon_\theta(x_t). \quad (\text{S14})$$

Substituting the expressions for conditional and unconditional noise predictions into this formulation yields:

$$\nabla_{x_t} \log p(x_t | y)_{\text{CFG}} = (1 + w)\left(\nabla_{x_t} \log p(x_t | y)\right) - w\left(\nabla_{x_t} \log p(x_t)\right), \quad (\text{S15})$$

which simplifies to:

$$\nabla_{x_t} \log p(x_t | y)_{\text{CFG}} = (1 + w)\nabla_{x_t} \log p(x_t | y) - w\nabla_{x_t} \log p(x_t). \quad (\text{S16})$$

This expression demonstrates how the guidance weight w governs the balance between the conditional and unconditional score functions. Specifically, when $w = 0$, the model reduces to the original conditional formulation. As w increases, the influence of the conditioning signal is amplified relative to the unconditional prediction. This flexibility allows for enhanced control over the trade-off between general empirical behavior and specific contextual dependencies, thus improving the model's ability to capture the desired runoff distribution.

Supplementary Text 2. Methodology for vapor pressure derivation and bias correction of CMIP6 daily variables using Distribution Mapping.

Vapor pressure

The processing of CMIP6 meteorological variables consisted of two main procedures: vapor pressure derivation and systematic bias correction. For vapor pressure calculation, we employed a two-step procedure utilizing daily near-surface air temperature (*tas*) and near-surface relative humidity (*hurs*) from CMIP6 outputs. Initially, the saturation vapor pressure (e_s) was calculated using the Buck equation^{S4}, which is extensively applied in atmospheric sciences:

$$e_s = 6.1121 \exp \left(\left(18.678 - \frac{T}{234.5} \right) \left(\frac{T}{257.14 + T} \right) \right), \quad (\text{S17})$$

where e_s is saturation vapor pressure (hPa) and T is temperature (°C) converted from *tas* (K). Subsequently, the actual vapor pressure (*vp*) was determined using relative humidity (*hurs*, %) through:

$$vp = \frac{hurs}{100} \cdot e_s. \quad (\text{S18})$$

Distribution Mapping

To address systematic biases in daily CMIP6 model outputs (precipitation, maximum and minimum temperature, solar radiation, and vapor pressure), we implemented the Distribution Mapping (DM) method^{S5}, which establishes a transfer function that adjusts the probability distribution of simulated climate variables to match that of observational data. The implementation began with fitting theoretical distributions to both historical observational data and model data from 1980–2014. Following Teutschbein and Seibert^{S6}, we employed different distributions based on the characteristics of meteorological variables. For daily precipitation, considering its non-negative and asymmetric distribution characteristics, we adopted the Gamma distribution:

$$f(x; \alpha, \beta) = \frac{\beta^\alpha}{\Gamma(\alpha)} x^{\alpha-1} e^{-\beta}, \quad x > 0, \quad (\text{S19})$$

where α and β denote the shape and scale parameters, respectively, and $\Gamma(\alpha)$ represents the Gamma function. For temperature (maximum and minimum), solar radiation, and vapor pressure, we utilized the Gaussian distribution:

$$f(x; \mu, \sigma) = \frac{1}{\sigma\sqrt{2\pi}} e^{-\frac{(x-\mu)^2}{2\sigma^2}}, \quad (\text{S20})$$

where μ and σ represent the location and scale parameters, respectively. The correction process was executed through mapping between theoretical distributions:

$$X_{corrected} = F_{obs}^{-1}(F_{mod}(X|\theta_{mod})|\theta_{obs}) \quad (\text{S21})$$

where F_{mod} and F_{obs}^{-1} represent the CDF of model data and inverse CDF of observational data, fitted with parameters θ_{mod} and θ_{obs} , respectively. To account for

seasonal variations in the distribution parameters, we performed the bias correction separately for each calendar month. Due to the lack of analytical solutions for inverse CDFs, we implemented numerical approximation using 99,999 uniformly distributed quantile points (ranging from 10^{-5} to 0.99999) for interpolation, ensuring accurate correction of extreme values. To preserve spatial heterogeneity, the correction procedure was independently performed for all 531 basins. Finally, the multi-model ensemble means for each scenario were derived by equally weighting the bias-corrected outputs from individual models. The temporal evolution of key representative variables after bias correction is shown in Supplementary Fig. S5.

Supplementary Text 3. Evaluation metrics.

Continuous Ranked Probability Score (CRPS)

CRPS is a comprehensive metric for evaluating the accuracy of probabilistic forecasts. Unlike deterministic evaluation indicators, CRPS evaluates the entire forecast distribution rather than single-point predictions, which is formally defined as:

$$\text{CRPS} = \int_{-\infty}^{\infty} (P(y) - H(y - x_{\text{obs}}))^2 dy, \quad (\text{S22})$$

where $P(y)$ is the cumulative distribution function of the forecast, x_{obs} is the observed value, and $H(y - x_{\text{obs}})$ is the Heaviside step function that takes the value 0 for negative arguments and 1 for non-negative arguments. For practical applications with empirical distributions of finite support, a discrete approximation is used:

$$\text{CRPS} = \sum_{i=1}^n P(y_i)^2 \cdot I(y_i \leq x_{\text{obs}}) + \sum_{i=1}^n (P(y_i) - 1)^2 \cdot I(y_i > x_{\text{obs}}), \quad (\text{S23})$$

where y_i represents discrete forecast values, n is the number of such values, and $I(\cdot)$ is an indicator function. To evaluate forecast performance over an extended period, the average CRPS is calculated as:

$$\text{CRPS}_{\text{avg}} = \frac{1}{T} \sum_{t=1}^T \text{CRPS}_t, \quad (\text{S24})$$

where T denotes the number of time points in the evaluation period. Notably, CRPS reduces to the Mean Absolute Error (MAE) when the forecast ensemble consists of a single member, making it a generalization of MAE for probabilistic forecasts.

Kling-Gupta Efficiency (KGE)

$$\text{KGE} = 1 - \sqrt{(r - 1)^2 + (\alpha - 1)^2 + (\beta - 1)^2}, \quad (\text{S25})$$

where r is the Pearson correlation coefficient, α is the ratio of simulated to observed standard deviation, and β is the ratio of simulated to observed mean. KGE provides a comprehensive evaluation that combines correlation, bias, and variability.

Nash-Sutcliffe Efficiency (NSE)

$$\text{NSE} = 1 - \frac{\sum(Q_{\text{obs}} - Q_{\text{sim}})^2}{\sum(Q_{\text{obs}} - \overline{Q_{\text{obs}}})^2}, \quad (\text{S26})$$

where Q_{obs} and Q_{sim} are the observed and simulated streamflow values, respectively, and $\overline{Q_{\text{obs}}}$ represents the mean of observed values. NSE evaluates the model's overall predictive skill relative to using the observed mean.

Alpha-NSE (α -NSE)

$$\alpha\text{-NSE} = \frac{\sigma_{\text{sim}}}{\sigma_{\text{obs}}}, \quad (\text{S27})$$

where σ_{sim} and σ_{obs} represent the standard deviation of simulated and observed values, respectively. α -NSE specifically assesses the model's ability to capture flow variability.

Beta-NSE (β -NSE)

$$\beta\text{-NSE} = \frac{\mu_{\text{sim}} - \mu_{\text{obs}}}{\sigma_{\text{obs}}}, \quad (\text{S28})$$

where μ_{sim} and μ_{obs} represent the mean of simulated and observed values. β -NSE quantifies the systematic bias in flow prediction.

Pearson correlation coefficient (COR)

$$\text{COR} = \frac{\sum(Q_{\text{obs}} - \overline{Q_{\text{obs}}})(Q_{\text{sim}} - \overline{Q_{\text{sim}}})}{\sigma_{\text{obs}}\sigma_{\text{sim}}}, \quad (\text{S29})$$

COR measures the linear correlation between simulated and observed flows.

Mean Absolute Error (MAE)

$$\text{MAE} = \frac{1}{n} \sum_{i=1}^n |Q_{\text{obs},i} - Q_{\text{sim},i}|, \quad (\text{S30})$$

where $Q_{\text{obs},i}$ and $Q_{\text{sim},i}$ represent observed and simulated values at time step i , respectively, and n is the total number of time steps. MAE quantifies the average magnitude of prediction errors without considering their direction.

Bias in flow duration curve high-segment volume (FHV)

$$\text{FHV} = \frac{\sum Q_{\text{sim},p} - \sum Q_{\text{obs},p}}{\sum Q_{\text{obs},p}} \times 100\%, \quad (\text{S31})$$

where p denotes values exceeding the 98th percentile. FHV focuses on evaluating the model performance during high-flow periods.

Bias in flow duration curve low-segment volume (FLV)

$$\text{FLV} = -1 \times \frac{(\sum \ln Q_{\text{sim},l} - \ln Q_{\text{sim},\min}) - (\sum \ln Q_{\text{obs},l} - \ln Q_{\text{obs},\min})}{\sum \ln Q_{\text{obs},l} - \ln Q_{\text{obs},\min}} \times 100\%, \quad (\text{S32})$$

where l represents values below the 30th percentile, and \min denotes the minimum value. FLV assesses the model's capability in simulating low-flow conditions.

Bias in the midsegment slope of flow duration curve (FMS)

$$\text{FMS} = \frac{(\ln Q_{\text{sim},l} - \ln Q_{\text{sim},u}) - (\ln Q_{\text{obs},l} - \ln Q_{\text{obs},u})}{\ln Q_{\text{obs},l} - \ln Q_{\text{obs},u}} \times 100\%, \quad (\text{S33})$$

where l and u represent the lower (20th) and upper (80th) percentiles, respectively. FMS evaluates the model's representation of flow variability in the middle range.

Peak-Timing error (P-T)

$$\text{P-T} = \frac{1}{n} \sum_{i=1}^n |t_{\text{obs},i} - t_{\text{sim},i}|, \quad (\text{S34})$$

where $t_{\text{obs},i}$ and $t_{\text{sim},i}$ are the timing of the i th observed and simulated peaks, respectively, and n is the total number of identified peaks. P-T quantifies the average temporal mismatch between simulated and observed peak flows.

Precision, recall, and F1 score

Precision, Recall, and F1 Score constitute fundamental metrics for evaluating flood forecasting systems, providing a nuanced evaluation that accounts for both false alarms and missed events. In the context of flood forecasting, a prediction is considered accurate when both observed and forecasted peak flows occur within the same natural day and exceed the flow threshold corresponding to the specified return period. These metrics are formally defined as follows:

$$\text{Precision} = \frac{\text{TP}}{\text{TP} + \text{FP}}, \quad (\text{S35})$$

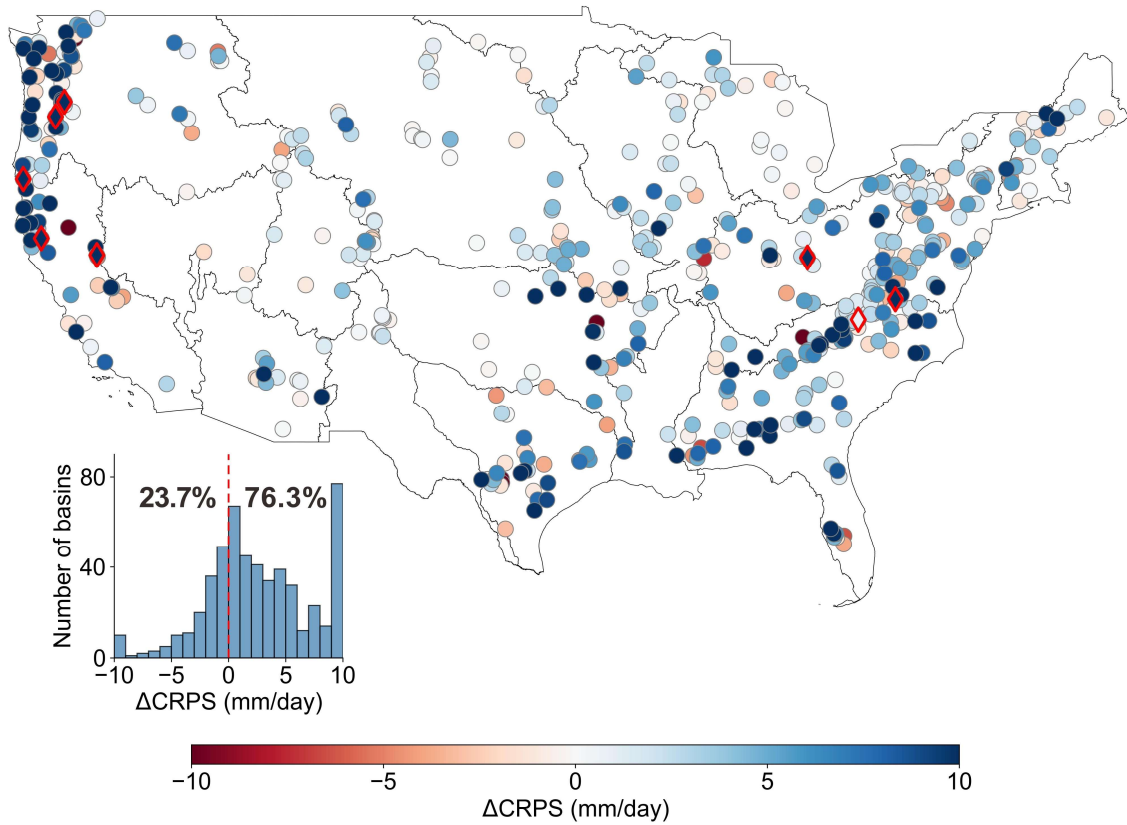
where TP represents true positives (correctly predicted flood events), and FP denotes false positives (incorrectly predicted flood events, or false alarms). Precision quantifies the proportion of correctly predicted flood events among all predicted flood events, indicating the trustworthiness of positive predictions.

$$\text{Recall} = \frac{\text{TP}}{\text{TP} + \text{FN}}, \quad (\text{S36})$$

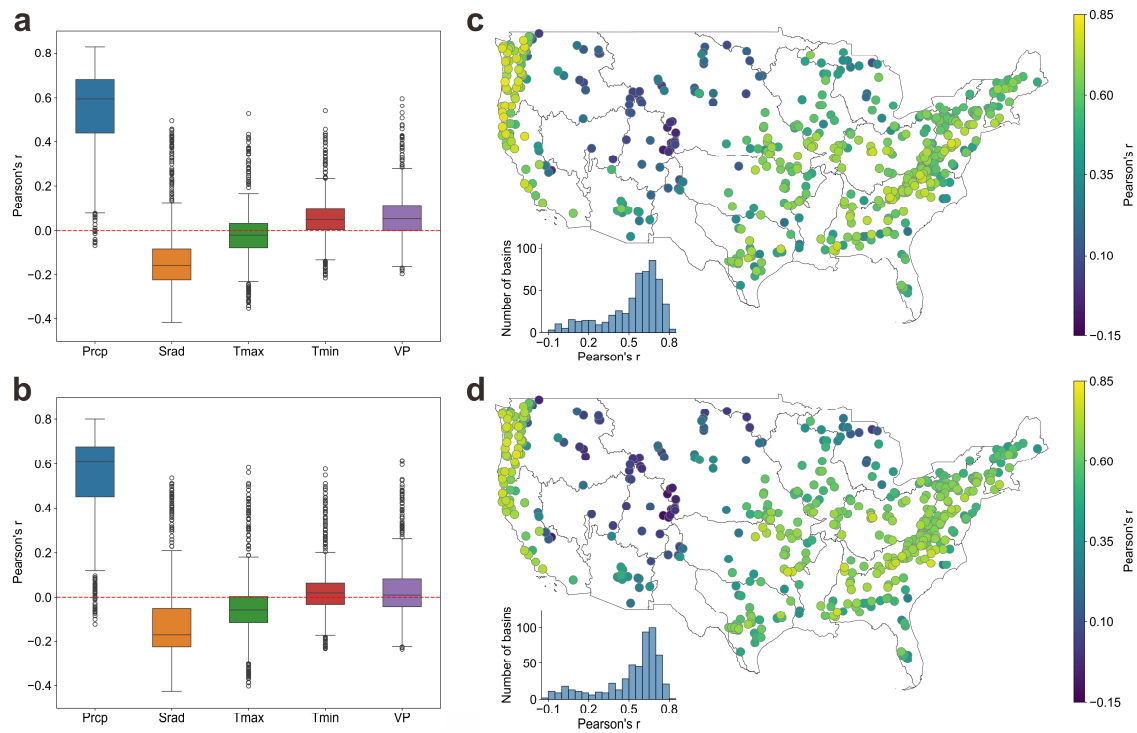
where FN represents false negatives (missed flood events). Recall, also known as sensitivity or true positive rate, measures the proportion of actual flood events that were correctly predicted, providing insight into the model's detection capability.

$$\text{F1 score} = 2 \times \frac{\text{Precision} \cdot \text{Recall}}{\text{Precision} + \text{Recall}} = \frac{2\text{TP}}{2\text{TP} + \text{FP} + \text{FN}}. \quad (\text{S37})$$

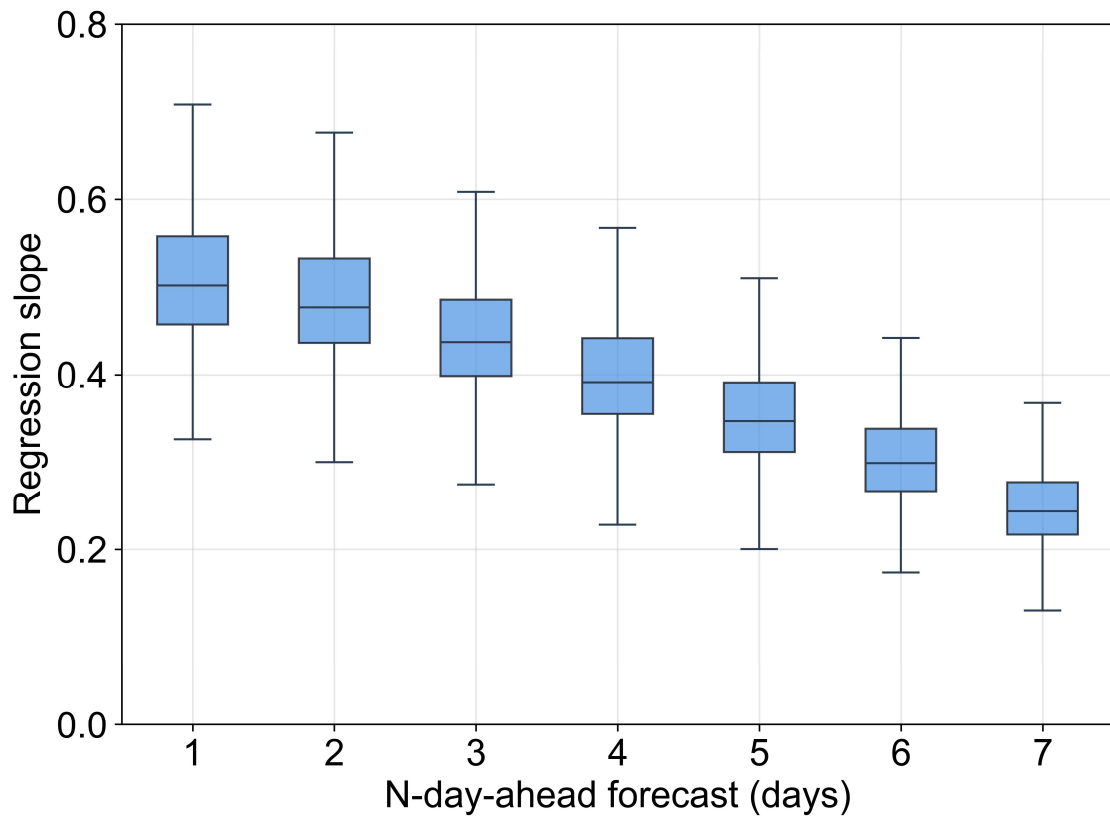
The F1 Score combines precision and recall into a single metric, offering a balanced assessment of the forecast system's performance. These metrics are typically calculated over an extended evaluation period, providing a comprehensive view of the forecasting system's capabilities across various conditions.



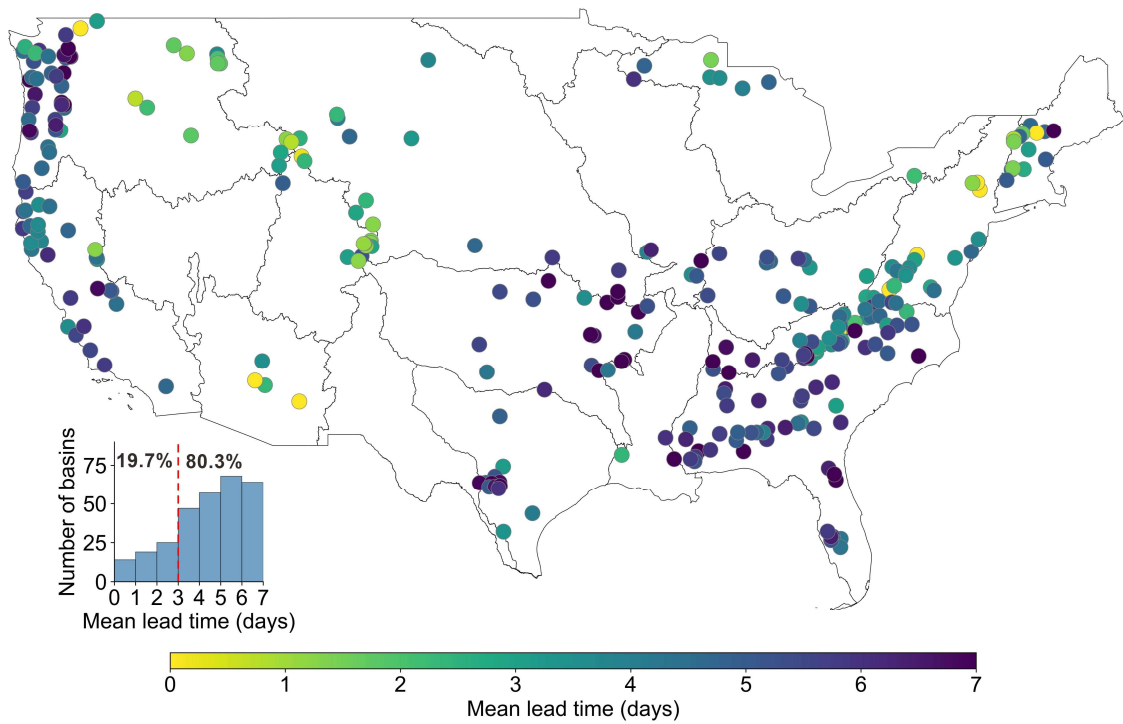
Supplementary Fig. S1. Probabilistic forecasting skill comparison between DRUM and LSTM-d. Spatial distribution of CRPS difference ($\Delta\text{CRPS} = \text{LSTM-d} \text{ minus DRUM}$) for the top 1% of flow events, where positive values indicate superior DRUM performance. Inset shows the ΔCRPS distribution truncated to $[-10, 10]$ for visualization clarity.



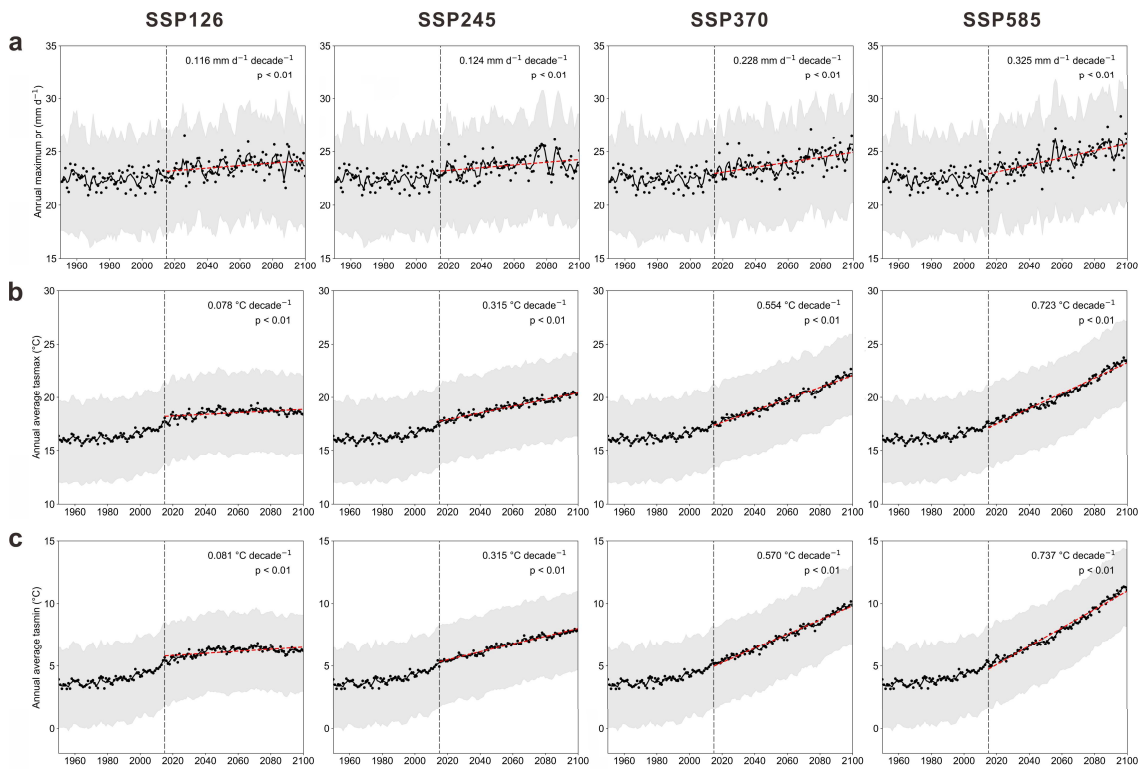
Supplementary Fig. S2. Relationships between uncertainty and meteorological forcings in probabilistic models. **a,b**, Correlation distributions between model uncertainty and meteorological forcings for DRUM (**a**) and LSTM-p (**b**). Box plots show median, interquartile range (IQR), and $1.5 \times \text{IQR}$ whiskers, with outliers as points. Forcings include precipitation (Prcp), solar radiation (Srad), temperature extremes (Tmax, Tmin), and vapor pressure (VP). Red dashed lines indicate zero correlation. **c,d**, Spatial patterns of precipitation-uncertainty correlation for DRUM (**c**) and LSTM-p (**d**), with frequency distributions shown in insets.



Supplementary Fig. S3. Distribution of regression slopes between observed and forecasted precipitation across 531 representative basins. For each forecast horizon (1–7 days), regression slopes were obtained by fitting a linear model ($y = ax + b$) between forecasted (y) and observed (x) daily precipitation, where slope < 1 indicate systematic underestimation of precipitation in forecasts. Each box depicts the interquartile range with a horizontal line indicating the median slope. Whiskers extend to 1.5 times the interquartile range. Outliers are omitted for visual clarity.



Supplementary Fig. S4. Flood warning capabilities in high-risk basins under climate change. For basins projected to experience increased flood risk in SSP585 scenario (as identified in Fig. 6d), spatial distribution of theoretical maximum lead times under perfect precipitation forecasts. Points are colored by mean lead time (days), computed as the average of maximum lead times across all flood events (lead time = 0 for missed events).



Supplementary Fig. S5. Temporal evolution of key meteorological variables under different SSP scenarios from 1950 to 2100. a,b,c, Time series of (a) annual maximum precipitation, (b) annual mean maximum temperature, and (c) annual mean minimum temperature under four SSP scenarios. Each point represents annual value. Black solid lines show smoothed time series using a 3-year moving average. Red dashed lines indicate fitted trends estimated by linear regression using time as the predictor variable, with significance levels (two-tailed Student's t-test) shown in the upper right corner of each panel. Gray shading indicates the interquartile range (25th to 75th percentiles) of the model ensemble. The vertical dashed line separates the historical period and future projections.

Supplementary Table S1. Comprehensive overview of CAMELS static catchment attributes.

Category	Attribute	Description	Unit
Climatic	p_mean	Mean daily precipitation.	mm/year
	pet_mean	Mean daily potential evapotranspiration.	mm/year
	aridity	Ratio of mean PET to mean precipitation.	-
	p_seasonality	Seasonality and timing of precipitation.	-
	high_prec_freq	Frequency of high precipitation days (≥ 5 times mean daily precipitation).	days/year
	low_prec_freq	Frequency of dry days (< 1 mm/day).	days/year
	high_prec_dur	Average duration of high precipitation events (number of consecutive days ≥ 5 times mean daily precipitation).	days
	low_prec_dur	Average duration of dry periods (number of consecutive days < 1 mm/day).	days
	frac_snow	Fraction of precipitation falling as snow (i.e., on days colder than 0°C).	-
Geological	carbonate_rocks_frac	Fraction of carbonate sedimentary rocks.	-
	geol_permeability	Subsurface permeability (\log_{10}).	m^2
Land cover	frac_forest	Forest fraction.	-
	lai_max	Maximum monthly mean of the leaf area index (based on 12 monthly means).	-
	lai_diff	Difference between the maximum and minimum monthly mean of the leaf area index (based on 12 monthly means).	-
	gvf_diff	Difference between the maximum and minimum monthly mean of the green vegetation fraction (based on 12 monthly means).	-
	gvf_max	Maximum monthly mean of the green vegetation fraction (based on 12 monthly means).	-

Soil	sand_frac	Sand fraction (of the soil material smaller than 2 mm, layers marked as oragnic material, water, bedrock and “other” were excluded).	%
	silt_frac	Silt fraction (of the soil material smaller than 2 mm, layers marked as oragnic material, water, bedrock and “other” were excluded).	%
	clay_frac	Clay fraction (of the soil material smaller than 2 mm, layers marked as oragnic material, water, bedrock and “other” were excluded).	%
	soil_depth_statsgo	Soil depth (maximum 1.5m, layers marked as water and bedrock were excluded).	m
	soil_porosity	Volumetric porosity (saturated volumetric water content estimated using a multiple linear regression based on sand and clay fraction for the layers marked as USDA soil texture class).	-
	soil_depth_pelletier	Depth to bedrock (maximum 50m).	m
	soil_conductivity	Saturated hydraulic conductivity (estimated using a multiple linear regression based on sand and clay fraction for the layers marked as USDA soil texture class).	cm/hr
	max_water_content	Maximum water content (combination of porosity and soil_depth_statgso, layers marked as water, bedrock and “other” were excluded).	m
Topographic	area_gages2	Catchment area (GAGESII estimate).	km ²
	elev_mean	Catchment mean elevation.	m
	slope_mean	Catchment mean slope.	m/km

Supplementary Table S2. Data availability of daily meteorological variables across CMIP6 GCMs under different scenarios. "√" represents temporally continuous daily data, "×" represents no data available; historical period spans 1950–2014, and future scenarios (SSPs) span 2015–2100.

Model	Variable	Historical	SSP126	SSP245	SSP370	SSP585
CanESM5	pr ^a	√	√	√	√	√
	tas ^b	√	√	√	√	√
	tasmax ^c	√	√	√	√	√
	tasmin ^d	√	√	√	√	√
	rsds ^e	√	√	√	√	√
	hurs ^f	√	√	√	√	√
CESM2	pr	√	√	√	√	√
	tas	√	√	√	√	√
	tasmax	×	×	×	×	×
	tasmin	×	×	×	×	×
	rsds	√	√	√	√	√
	hurs	√	√	√	√	√
CNRM-CM6-1	pr	√	√	√	√	√
	tas	√	√	√	√	√
	tasmax	√	√	√	√	√
	tasmin	√	√	√	√	√
	rsds	√	√	√	√	√
	hurs	√	√	√	√	√
EC-Earth3	pr	√	√	√	√	√
	tas	√	√	√	√	√
	tasmax	√	√	√	√	√
	tasmin	√	√	√	√	√
	rsds	√	√	√	√	√
	hurs	√	√	√	√	√
MPI-ESM1-2-HR	pr	√	√	√	√	√
	tas	√	√	√	√	√
	tasmax	√	√	√	√	√
	tasmin	√	√	√	√	√
	rsds	√	√	√	√	√
	hurs	√	√	√	√	√

^a Mean of the daily precipitation rate ($\text{kg m}^{-2} \text{s}^{-1}$); ^b Daily near-surface air temperature (K); ^c Daily maximum near-surface air temperature (K); ^d Daily minimum near-surface air temperature (K); ^e Surface downwelling shortwave radiation (W m^{-2}); ^f Near-surface relative humidity (%).

Supplementary Table S3. Configurations of model architectures and training settings.

Configuration	DRUM	LSTM-d	LSTM-p
Architecture			
Backbone	Encoder-decoder LSTM	Encoder-decoder LSTM	Encoder-decoder LSTM
Number of layers	1	1	1
Hidden size	256	256	256
Dropout rate	0.5	0.5	0.5
Input	365-day Meteorological time series (precipitation, maximum and minimum temperature, shortwave radiation, and vapor pressure) Catchment characteristics (27 static attributes) Future precipitation forecasts (aligned with prediction horizon)		
Output	Mean and variance of reverse process at each step	Deterministic values	ALD parameters (μ , σ , τ)
Training			
Input standardization	Yes	Yes	Yes
Optimizer	Adam	Adam	Adam
Batch size	256	256	256
Total epochs	200	30	60
Learning rate schedule	1e-4 (100 epochs) 5e-5 (40 epochs) 1e-5 (40 epochs) 5e-6 (20 epochs)	1e-3 (10 epochs) 5e-4 (10 epochs) 1e-4 (10 epochs)	5e-4 (30 epochs) 1e-4 (30 epochs)
Loss function	Diffusion loss	NSE*	Negative log-likelihood of ALD

Supplementary Reference

- S1. Ho, J., Jain, A., & Abbeel, P. (2020). Denoising diffusion probabilistic models. *Advances in neural information processing systems*, 33, 6840-6851.
- S2. Song, Y., & Ermon, S. (2019). Generative modeling by estimating gradients of the data distribution. *Advances in neural information processing systems*, 32.
- S3. Ho, J., & Salimans, T. (2022). Classifier-free diffusion guidance. *arXiv preprint arXiv:2207.12598*.
- S4. Buck, A. L. (1981). New equations for computing vapor pressure and enhancement factor. *Journal of Applied Meteorology* (1962-1982), 1527-1532.
- S5. Sennikovs, J., & Bethers, U. (2009, July). Statistical downscaling method of regional climate model results for hydrological modelling. In *Proceedings of the 18th World IMacS/MODSIM congress* (pp. 3962-3968).
- S6. Teutschbein, C., & Seibert, J. (2012). Bias correction of regional climate model simulations for hydrological climate-change impact studies: Review and evaluation of different methods. *Journal of hydrology*, 456, 12-29. <https://doi.org/10.1016/j.jhydrol.2012.05.052>.